Multiple ocean oxygenation events during the Ediacaran Period: Mo isotope evidence from the Nanhua Basin, South China

Lin Yuan[a,*], Ying Zhou[a,*], Xi Chen[a,b], Maoyan Zhu[c,d], Simon W. Poulton[e], Zheyu Tian[a], Da Li[f], Matthew Thirlwall[g], Graham A. Shields[a]

[a]*Department of Earth Sciences, University College London, London, WC1E 6BT, UK*

[b]*Laboratory for Mineral Deposits Research, School of Earth Sciences and Engineering, Nanjing University, Nanjing 210023, China*

[c]*State Key Laboratory of Palaeobiology and Stratigraphy and Center for Excellence in Life and Paleoenvironment, Nanjing Institute of Geology and Palaeontology, Chinese Academy of Sciences, Nanjing 210008, China*

[d]*College of Earth and Planetary Sciences, University of Chinese Academy of Sciences, Beijing 100049, China*

[e]*School of Earth and Environment, University of Leeds, Leeds, LS2 9JT, UK*

[f]*School of Marine Science and Engineering, Nanjing Normal University, Nanjing 210023, Jiangsu, China*

[g]*Department of Earth Sciences, Royal Holloway, University of London, Egham, TW20 0EX*

*Corresponding authors at: Department of Earth Sciences, University College London, Gower Street, London, UK, WC1E 6BT

E-mail address: lin.yuan.19@ucl.ac.uk (Lin Yuan); y-zhou@ucl.ac.uk (Ying Zhou)

Abstract

The Ediacaran Period (ca. 635–539 Ma) was an eventful interval in Earth history, during which a succession of biological and environmental changes, including episodic ocean oxygenation events (OOEs), paved the way for the Cambrian radiations of animal life. To better understand the evolution of ocean redox conditions and to estimate the extent of seafloor oxygenation during this period, we analysed molybdenum (Mo) isotope compositions and redox sensitive element (RSE) concentrations from a continuous, mid-slope section of the Doushantuo Formation (ca. 635–560 Ma) of the Nanhua Basin on the South China Craton. Alongside an updated compilation of published Mo isotope and RSE data, our new data show that three OOEs occurred within a generally anoxic Ediacaran ocean, with the last, particularly extensive event occurring during deposition of Doushantuo Member IV. Here we show how the global balance of redox-related Mo sinks shifted dynamically in response to these transient OOEs, which correlate well with the first appearance of Ediacaran fossil groups and so may have triggered or stimulated biotic innovations and radiations. Moreover, the spatial distribution of the Mo data from multiple sections supports episodic expansion of a euxinic wedge on the slopes of the Nanhua Basin, consistent with pyrite burial as a potential cause of the OOEs.

Keywords: Ediacaran Period, molybdenum isotopes, redox sensitive elements, ocean oxygenation, Doushantuo Formation, Nanhua Basin

1. Introduction

The Ediacaran Period (~635–539 Ma) marks a turning point when several important evolutionary and environmental events occurred that set the stage for the subsequent progression towards the modern Earth system. This includes the appearance of complex multicellular eukaryotes in the form of the Ediacaran biota (Narbonne 2005; Droser et al., 2017), which reached its maximum diversity at around 560 Ma (Xiao et al., 2009). Most eukaryotes, especially the overwhelming majority of metazoans, require oxygen for various physiological processes (Summons et al., 2006; Acquisti et al., 2007; Narbonne 2004; Canfield et al., 2007, Sperling et al., 2013). In line with this, the diversification of animals has been plausibly linked to a stepwise rise in oceanic (and possibly atmospheric) oxygenation during the late Ediacaran Period (Canfield et al., 2007; Frei et al., 2009; Knoll, 2011; Lenton et al., 2014; Chen et al., 2015; Bowyer et al., 2017; Cole et al., 2020).

It is commonly thought that ca. 1.5 billion years after the 'Great Oxidation Event' (GOE, around 2.3 Ga) (Holland, 2002; Canfield, 2005), there was a second significant increase in Earth surface oxygen levels (termed the 'Neoproterozoic Oxygenation Event', NOE) at ~0.8–0.5 Ga (Shields-Zhou and Och, 2011). Indeed, it has been suggested that the extent of global seafloor oxygenation during the NOE may have risen to near present levels (Zhang et al., 2019). In more detail, however, abundant evidence shows that Ediacaran ocean oxygenation events (OOEs) were only transient (Canfield et al., 2007; Sahoo et al., 2012, 2016; Zhang et al., 2019; Xu et al., 2022), while ferruginous (Fe^{2+} containing) or euxinic (sulphidic) anoxic environments (Canfield et al., 2008; Li et al., 2010; Kurzweil et al., 2015; Wood et al., 2015; Zhang et al., 2018) continued to be widespread. Although enrichments of redox-sensitive element (RSE) on the South China Craton (particularly the Doushantuo Formation) imply

that oceans were widely oxygenated following Marinoan glaciation (Sahoo et al., 2012, 2016), the oxygenation level likely waxed and waned throughout the NOE interval (Fike et al., 2006; Canfield et al., 2008; McFadden et al., 2008; Kendall et al., 2015; Sperling et al., 2015; Tostevin et al., 2019; Tostevin and Mills, 2020; Wei et al., 2021). Furthermore, oceanic redox structure, especially around productive margins, may have been highly variable (Li et al., 2015). Overall, the detailed timing and intensity of Ediacaran oxygenation, as well as resultant changes in the marine redox landscape, remain unclear (Och and Shields-Zhou, 2012; Sperling et al., 2013; Lyons et al., 2014; Och et al., 2016). Thus, further detailed studies utilising redox proxies that address local to more regional redox heterogeneity are required.

Here, we present and interpret a local to potentially global redox proxy dataset, including Fe-speciation, RSEs, and Mo isotopes, from a newly discovered and dated mid-slope section named Xiajiaomeng West (XJMW), Guizhou Province, South China. Combined with data from previous studies on Ediacaran sections positioned at various water depths across the Nanhua Basin, these new data from the Doushantuo Formation provide supporting evidence for the occurrence of OOEs through the Ediacaran Period, and allow a detailed investigation of the temporal and spatial evolution of redox conditions on productive ocean margins during the Ediacaran Period.

2. Background: Geochemical proxies

A sequential extraction procedure for acquiring the relative proportion of iron mineral species in ancient sediments, iron speciation, is widely used to investigate the local to regional redox state of ocean basins (Poulton and Canfield, 2005; 2011). The ratio of Fe_{HR}/Fe_T (Fe_{HR}, highly reactive iron,

89 normalised to Fe_T, total iron) has been extensively calibrated as a tool to identify water column anoxia
90 in ancient marine settings (Raiswell and Canfield, 1998; Raiswell et al., 2001; Poulton and Raiswell,
91 2002; Clarkson et al., 2014). Fe_{HR}/Fe_T ratios below 0.22 suggest probable oxic water column conditions,
92 while $Fe_{HR}/Fe_T > 0.38$ implies water column anoxia, with intermediate Fe_{HR}/Fe_T ratios considered
93 equivocal (Poulton and Canfield, 2011). For anoxic conditions, euxinia can be distinguished from
94 ferruginous conditions by considering the extent of the pyritisation of the highly reactive iron pool
95 (Fe_{Py}/Fe_{HR}; Poulton et al., 2004; Poulton and Canfield, 2011). Recent work on the euxinic Lake Cadagno
96 (Xiong et al., 2019) and euxinic Holocene sediments from the Eastern Mediterranean Sea (Benkovitz
97 et al., 2020), combined with existing criteria (Anderson and Raiswell, 2004; März et al., 2008), suggest
98 that $Fe_{Py}/Fe_{HR} < 0.6$ provides strong support for ferruginous water column conditions, $Fe_{Py}/Fe_{HR} > 0.8$
99 implies euxinic conditions, while ratios of 0.6−0.8 are considered equivocal and require additional
100 evidence, such as trace metal concentrations and isotope compositions, to interpret the precise redox
101 state of the water column (Poulton, 2021).

102 Redox-sensitive element concentrations are used for tracing not only local but also global ocean
103 redox states (Sahoo et al., 2012, 2016; Ostrander et al., 2019). Most RSEs are transferred to the ocean
104 in the form of aqueous oxyanions derived from the oxidative weathering of RSE-bearing minerals
105 (Dunk et al., 2002; Miller et al., 2011), while marine sediments represent the RSE sinks with variable
106 RSE accumulation rates governed largely by the redox condition of the local depositional environment.
107 RSE contents in marine sediments beneath oxic waters generally approximate crustal values (Mo ~1.1
108 ppm, U ~1.7 ppm, V ~98 ppm; Wedepohl, 1995) without authigenic enrichment, as most of the RSEs
109 remain in dissolved form in oxic seawater, which today has Mo ~110 nM (Ho et al., 2018), U ~14 nM,
110 and V ~40 nM (Morford and Emerson, 1999). The exception is authigenic Fe-Mn oxides, onto which

RSEs, Mo and V in particular, may be sequestered via adsorption (Tribovillard et al., 2006).

Under reducing marine states, the burial fluxes of many RSEs (e.g., Mo, U and V) exceed those in oxygenated settings by several orders of magnitude (Sahoo et al., 2012). Under anoxic (both sulphidic and ferruginous) conditions, dissolved U may be efficiently deposited, following reduction from U(VI) to U(IV) (Tribovillard et al., 2012; Massey et al., 2014; Brüske et al., 2020). Similarly, under suboxic or anoxic conditions, pentavalent vanadate is reduced to tetravalent vanadyl susceptible to incorporation into organic matter (Breit and Wanty, 1991). Further reduction to insoluble trivalent V species is kinetically slow (Wanty and Goldhaber, 1992) and does not induce sedimentary V enrichment, even in the modern euxinic Framvaren Fjord, which has the highest marine H_2S concentration of 8 mM (Scott et al., 2017). By contrast, Mo precipitation initiates due to thiolation by H_2S, rather than reduction, and thiomolybdates are prone to further particle scavenging (Helz et al., 1996) or sulphide formation (Helz, 2021).

As RSE enrichments in anoxic marine sediments generally report dissolved RSE availabilities, they can be applied to trace ocean redox state (Scott et al., 2008; Algeo et al.,2006; Och and Shields-Zhou, 2012). Both global and local factors affect the extent of RSE availabilities including, particularly, the content of these elements in the open ocean, as well as the connectivity of ocean basins to the open ocean (Algeo and Maynard, 2004; Lyons and Severmann, 2006). Basin restriction generally reduces the extent of RSE enrichments (Algeo et al; 2006; Lyons et al, 2009), which means that the upper limits of enrichments within an interval indicate the RSE availabilities within the least restricted basin, so that they do not only have local significance (Sahoo et al., 2012). Therefore, high RSE enrichments recorded in euxinic shales provide strong evidence for a broadly oxygenated ocean, since such enrichments in locally anoxic settings require high availability of RSE sourced from a largely

oxygenated open ocean (Scott et al., 2008; Sahoo et al., 2012, 2016).

Molybdenum (Mo) isotopes have developed into a strong palaeoredox proxy for evaluating the spatial extent of different oceanic redox conditions, due to the redox controlled switches between different depositional mechanisms and ensuing changes in isotope fractionations (e.g., Anbar, 2004; Arnold et al., 2004; Kendall et al., 2017). In the modern oxygenated ocean, Mo scavenging by Fe-Mn oxides comprises a large portion of the global Mo sink. This process is slow, and Fe-Mn oxides are significantly enriched in the lighter Mo isotopes (Barling et al., 2001), which causes modern open ocean seawater (OSW) to be homogeneously enriched in the heavier Mo isotopes, with a $\delta^{98}Mo_{OSW}$ composition of around +2.34‰ (Nakagawa et al., 2012).

Similarly, high $\delta^{98}Mo$ values have been reported from sediments deposited during the early Cambrian (Chen et al., 2015), early Devonian (Dahl et al., 2010), and the Palaeocene–Eocene thermal maximum (Dickson et al., 2012), and are interpreted to reflect a modern-like extent of oxygenated seafloor. These interpretations are based on the observation that isotopic fractionations are commonly much smaller under suboxic through to anoxic conditions (Poulson et al., 2009). When the bottom waters are more reducing, or when organic burial and microbial sulphate reduction (MSR) rates are higher, the generation of dissolved sulphide results in conversion of molybdate to thiomolybdate species. Both theoretical calculations (Tossell, 2005) and experimental observations (Kerl et al., 2017; Hlohowskyj et al., 2021) indicate large isotopic fractionations between thiomolybdate species ($MoO_xS_{4-x}^{2-}$). The products of higher degrees of thiolation tend to incorporate more of the lighter Mo isotopes and are more susceptible to scavenging by solid phases (Erickson and Helz 2000). Therefore, incomplete removal of more sulphidised thiomolybdate species from seawater to the sediments can cause low $\delta^{98}Mo_{sed}$ values. The $\delta^{98}Mo_{sed}$ value approaches $\delta^{98}Mo_{OSW}$ when H_2S

155 increases and removal of thiomolybdates becomes more quantitative. Therefore, when ocean anoxia
156 expands, the $\delta^{98}Mo_{OSW}$ value tends to decrease, as shown near the end of the Permian Period (Zhang
157 et al., 2021) and during the Late Cretaceous Ocean Anoxic Event (OAE) 2 (Goldberg et al., 2016;
158 Dickson et al., 2021).
159
160

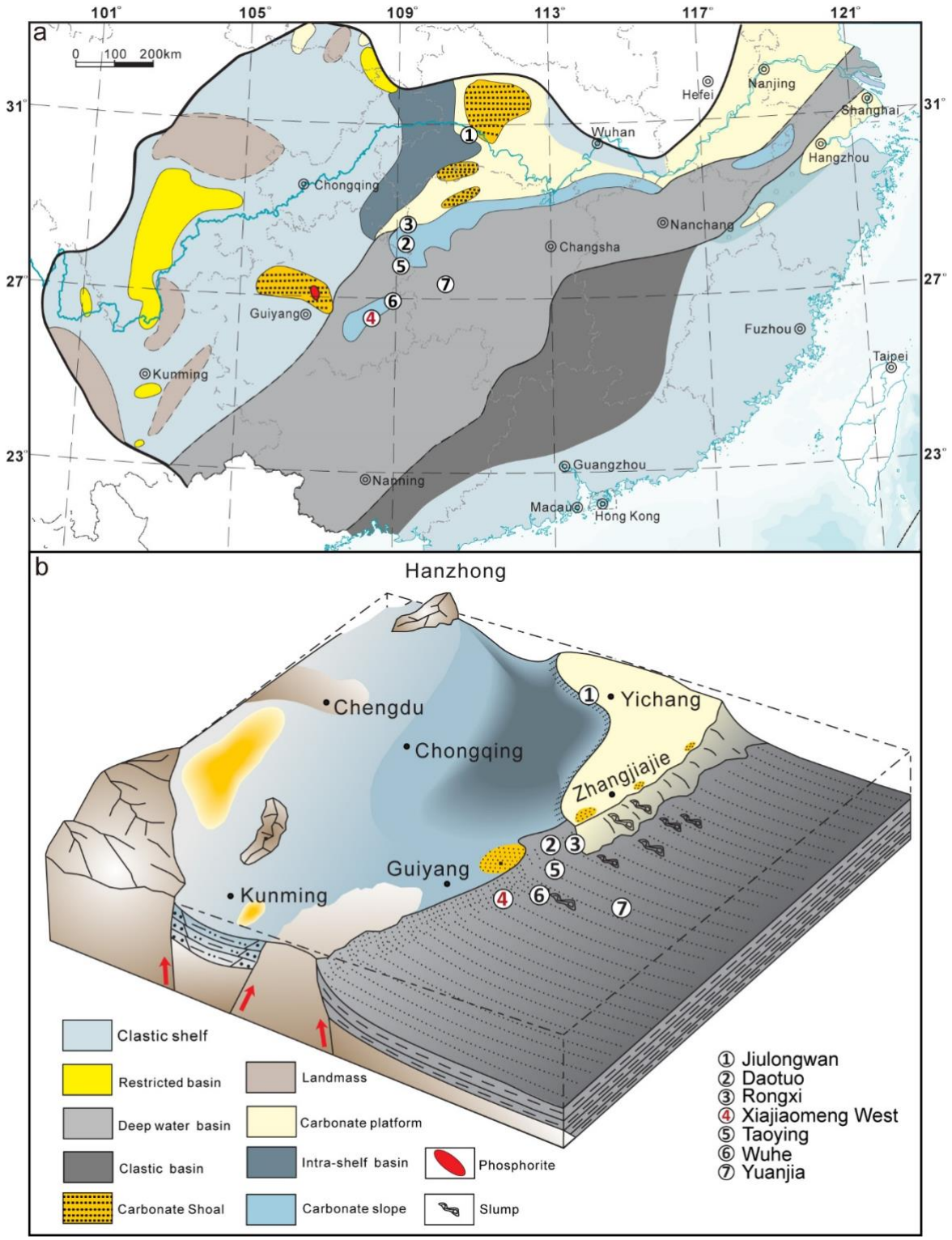

Fig. 1. (a) A reconstructed paleogeographic map of South China Craton during the deposition time of Doushantuo Formation, modified from Lu et al. (2013). (b) A 3D paleogeographic reconstruction of the Nanhua Basin together with the depositional environment. The figure is modified from Zhu et al.

(2019) and see the legend of color in the reference paper.

3. Study sites and samples

3.1. The Doushantuo Formation on the South China Craton

The South China Craton consists of two blocks, Yangtze and Cathaysia, between which the Nanhua Basin developed as a failed intra-cratonic rift basin at ~820 Ma (Wang and Li, 2003). Ediacaran sedimentary successions, comprising the Doushantuo and Dengying formations, are well preserved over the Yangtze platform, with the underlying Doushantuo Formation representing a considerably greater proportion of Ediacaran time (Condon et al., 2005). The Nanhua Basin comprises a large platform facies, a transition belt, and a basin facies, representing a shelf-to-basin transect from the northwest to the southeast (Fig. 1a and 1b). The precise palaeobathymetric reconstructions of Zhu et al. (2003) have reflected that the shallow-water platform was characterised by multiple intra-shelf basins and carbonate barriers on its margins. The Doushantuo Formation was deposited on the south-eastern margin of the Yangtze platform with some connection to the open ocean (Jiang et al., 2011; Sahoo et al., 2012). It is underlain by the Nantuo Formation, which mainly comprises glacigenic diamictites deposited towards the end of the Cryogenian Period, and is overlain by the Dengying/Liuchapo formations that were deposited during the terminal part of the Ediacaran Period.

The Doushantuo Formation in the Yangtze Gorges area has been commonly divided into four distinct lithological members (I–IV from base to top), which are likely correlative with sections of the

same formation name along the basin margin (McFadden et al., 2008; Jiang et al., 2011). Member I, a cap carbonate (dolostone), overlies the Nantuo diamictite and can be up to ~5 m thick in the Yangtze Gorges area. There is an ash bed just above the top of Member I in the Yangtze Gorges area which has been dated at 635.23 ± 0.57 Ma (Condon et al., 2005), with a 634.57 ± 0.88 Ma age from the uppermost Nantuo Formation (Zhou et al., 2019). These two ages are similar to ages from other well-known basal Ediacaran sections, including <636.41 ± 0.45 Ma from Tasmania, Australia (Calver et al., 2013), <635.21 ± 0.59 Ma in northern Namibia (Prave et al., 2016), and >632.3 ± 5.9 Ma in northwestern Canada (Rooney et al., 2015). The two ages from the South China Craton are almost indistinguishable within analytical error, and together they indicate that the boundary of Cryogenian–Ediacaran is at approximately 635 Ma (Xiao and Narbonne, 2020).

Member II comprises interbedded black shale and dolostone with abundant chert nodules and pyrite. U-Pb zircon dating from about six meters from the base of this member gives an age of ~632 Ma (Condon et al., 2005). Member III is mainly composed of carbonates, largely ribbon-banded limestones and marls, with irregular chert bands and fewer shale layers. Member IV is dominated by organic-rich black shale, which is overlain by the Dengying/Liuchapo Formation. The end of Member IV deposition at the Jiuqunao (Jijiawan) section in the Yangtze Gorges area is dated by a zircon age of ~551 Ma from an ash layer, which was reported to be 1 m below the top of Member IV (Condon et al., 2005; Zhang et al., 2005). More recently, this has been re-dated to 550.1 ± 0.6 Ma by Yang et al. (2021). In the Doushantuo Formation, biostratigraphic correlations can be made using fossil assemblages, including macroscopic carbonaceous compressions of multicellular algae, and acanthomorphic acritarchs (Xiao et al., 2004; Yuan et al., 2011; Xiao et al., 2014; Qu et al., 2018; Quyang et al., 2019). The overlying Dengying/Liuchapo Formation preserves biomineralising

metazoan fossils, including the Shibantan and Gaojiashan biotas (Xiao et al., 2005; Cai et al., 2010; Chen et al., 2014).

The upper part of the Doushantuo Formation (Members III and IV) records a large, negative carbon isotope excursion, called the 'DOUshantuo Negative Carbon isotope Excursion' (DOUNCE) in South China (Lu et al., 2013). The top of Doushantuo Member IV marks the end of the DOUNCE (>~550 Ma; Yang et al., 2021) and this excursion is considered to be equivalent to the Shuram $\delta^{13}C$ excursion in Oman (Fike et al., 2006), the Wonoka $\delta^{13}C$ excursion in southern Australia (Calver, 2000), and the Krol B $\delta^{13}C$ excursion in northern India (Kaufman et al., 2006), all recorded from upper Ediacaran successions. Different models have been proposed to interpret extreme negative carbon isotope excursions, such as the remineralisation of a putative, large dissolved organic carbon pool (Rothman et al., 2003). However, Bristow and Kennedy (2008) pointed out that such an event would have exhausted ocean oxidant supply on a timescale of ~800 kyr, much shorter than the likely duration of the anomaly. This issue can potentially be resolved if surplus sulphate weathering coupled with pyrite burial replenished the requisite oxidant (Shields et al., 2019). Alternative models include authigenic carbonate deposition (Schrag et al., 2013; Laakso and Schrag 2020), while some argue for a local or diagenetic origin for the $\delta^{13}C$ excursions (e.g., Busch et al., 2022).

3.2 Studied section: Xiajiaomeng

The XJMW section (26°68'56''N, 108°33'82''E) is located in Guizhou Province and is ~70 km to the southwest of the Wuhe section (Fig. 1; red number). The XJMW section incorporates the whole of the Doushantuo Formation, and the lithologies vary from carbonates and calcareous dolomite to

232 shales. In total, 45 samples were collected from an abandoned quarry with freshly exposed surface.
233 Based on a lithological comparison with the four members of the Doushantuo Formation observed in
234 the Yangtze Gorges area, the Doushantuo Formation at XJMW can be similarly divided into four
235 members: Members I–IV. The dolomitic Member I sits above the Nantuo diamictite, and likely
236 represents the “cap dolostone” in this section; Member II begins with the first chert bed. Its lower
237 part is predominantly siliceous with some carbonate interbeds, becoming more shaly upwards, with
238 cherty interbeds; Member III is mostly carbonate with some chert bands; Member IV is dominated
239 by black shale or marl. Compared with Yangtze Gorges sections, the XJMW section appears to be
240 relatively more enriched in silicate minerals as shown by elevated Al contents (Table 1 and Fig. S1)
241 and was deposited in a middle slope environment in the Nanhua Basin (Fig. 1b).

242 The overall thickness of the sampled section is approximately 38 m, having been shortened
243 somewhat by tectonic shearing and low-grade, regional metamorphism. The only dating result for the
244 slope sections is a zircon U-Pb age of 556.4 $\pm$ 0.7 (CA-ID-TIMS) from the lower part of the overlying
245 Liuchapo Formation at the same XJMW section (Yang et al., 2021). This would be consistent with an
246 age of ~560 Ma for the end of Doushantuo Member IV. (Yang et al., 2021). For the purpose of this
247 study, we assume an age span of ~635 to ~560 Ma for the entire Doushantuo Formation and an
248 approximately constant sedimentation rate (Table 1). There is a negative carbon isotope excursion
249 found in Member III at the Xiajiaomeng section, and $\delta^{13}C$ reaches as low as −6.5‰ (Yang et al., 2021).
250
251
252 **4. Methodology**
253

All samples were crushed and ground into powder using a SIEBTECHNIK TEMA tungsten carbide mill. RSE concentrations were acquired by X-ray fluorescence (XRF) on a Philips PW2400 Spectrometer (PANalytical, Almelo, the Netherlands) at Royal Holloway University, London, with representative reproducibilities (2SD) of Mo = 0.2 ppm, U = 0.4 ppm, and V = 2.4 ppm. Fe extractions were conducted at the University of Leeds following the methods outlined in Poulton and Canfield (2005) and Canfield et al. (1986). The concentrations of Fe in operationally-defined sequential leaches of unsulphidised Fe phases (see Poulton, 2021) were determined by atomic absorption spectroscopy, while the concentration of pyrite Fe was determined gravimetrically after precipitation as Ag_2S. Replicate extractions gave a relative standard deviation of <5% for all steps, and accuracy was ensured using international Fe speciation standard, WHIT (Alcott et al., 2020). Total organic carbon (TOC) was obtained by the difference between total carbon before and after the removal of inorganic carbon (two 10% (vol/vol) HCl washes for 24 h). Samples were analysed on a FLASH EA elemental analyser at University College London, and replicate analyses gave a precision of ± 0.12 wt% (2SD).

Mo purification and δ^{98}Mo measurements were performed at Nanjing University, China. For Mo isotope analysis, about 10−100 mg of powder containing ~50−200 ng Mo was digested with HNO_3 and HF. A drop of ^{97}Mo–^{100}Mo double spike containing the same amount of Mo was added to the mixture. The mixture was left on a hotplate (150 °C) for ~72 h. The supernatant was separated and dried before being re-dissolved using HCl. The purification of Mo using BPHA resin follows the protocol of Li et al. (2014). Mo isotope compositions were measured on a Thermal Neptune Plus multi-collector ICP-MS. The measurement and mass bias correction by the double spike technique were carried out as described by Archer and Vance (2008). The Mo isotope data are reported relative to the reference standard, NIST-SRM-3134 (δ^{98}Mo = +0.25‰; Nägler et al., 2014). The internal

reproducibility of δ^{98}Mo measurements was better than 0.1‰ (2SE, n = 30).

To assess and compare the authigenic fractions of RSEs, enrichment factors (EFs) were calculated via the equation $X_{EF} = [(X/Al)_{sample} / (X/Al)_{UCC}]$ (Tribovillard et al., 2006; Algeo and Tribovillard, 2009), where X (ppm) and Al (wt%) represent the contents of RSE X and Al, respectively. Data are normalised against abundances of upper continental crust (UCC) outlined in McLennan (2001). In general, $X_{EF} > 3$ corresponds to a detectable authigenic enrichment, while $X_{EF} > 10$ suggests a substantial enrichment (Algeo and Tribovillard, 2009).

5. Results

5.1. Redox conditions at the XJMW section

For the XJMW section, all but two samples (XJMW33 and 39) had Fe_T contents above 0.5 wt%, which is considered to give a robust Fe speciation signal (Clarkson et al., 2014), and hence these samples were analysed for Fe speciation (Table 1). Almost all XJMW samples have Fe_{HR}/Fe_T ratios greater than 0.38, suggesting deposition beneath a persistently anoxic water column. The only exception is sample XJMW41, which had an Fe_{HR}/Fe_T ratio of 0.28 in the equivocal anoxic zone. However, the RSE contents of this sample are similar to those of neighbouring samples above and below, indicating probable anoxia (Table 1; Fig. 2). For Member I, Fe_{Py}/Fe_{HR} ratios for all samples were <0.6, indicating that Member I was deposited under a ferruginous water column. For Member II, the lower part shows a ferruginous signature with $Fe_{Py}/Fe_{HR} < 0.6$, while samples in the upper part lie mostly in the equivocal

zone, with Fe_{Py}/Fe_{HR} between 0.6 and 0.8, possibly fluctuating between ferruginous and euxinic conditions. The Fe_{Py}/Fe_{HR} values of Member III range between 0.26 and 0.89, showing oscillating euxinic and ferruginous values. In Member IV, except for XJMW41 (Table 1), all samples have equivocal (0.6−0.8) or euxinic Fe_{Py}/Fe_{HR} (>0.8) ratios.

5.2. RSE concentrations at the XJMW section

As shown in Fig. 2 and Table 1, the different measured redox sensitive elements (Mo, U, and V) show roughly the same trend. Based on elevated RSE concentrations, three distinct intervals of enrichment can be identified (Fig. 2): Interval A: basal Member II, Interval B: basal Member III, and Interval C: Member IV. The occurrence of these three RSE-enriched intervals is approximately consistent with previous studies of other sections across the basin transect (Kendall et al., 2015; Sahoo et al., 2016; Ostrander et al., 2019; Ye et al., 2020).

The first high RSE interval (Fig. 2; Table 1) occurs in basal Member II (Mo = 0.4−15 ppm, U = 3−15 ppm, V = 100−1200 ppm). Mo_{EF}, U_{EF}, and V_{EF} ranges are 1−9, 3−7, and 3−30, respectively. This interval is followed by a progressive shift to lower RSE concentrations from 7−25 m at the section (Mo = 2−4 ppm, U = 3−5 ppm, V = 80−120 ppm), with concentrations that are similar to crustal values (Mo = 1−2 ppm, U = 2−4 ppm, V = 120−140 ppm). At the base of Member III (Fig. 2; Interval B), RSE concentrations increase again, with Mo contents varying between 1−11 ppm (Mo_{EF} = 4−9), U between 1−11 ppm (U_{EF} = 2−6), and V between 21−160 ppm (V_{EF} = 1−2). Above this interval, RSE concentrations again decrease to near crustal levels. Finally, there is a third large shift in RSE concentrations in Member IV (Interval C), whereby this interval records the highest Mo and U concentrations (Mo =

6−312 ppm, U = 6−48 ppm), while V concentrations are also elevated (115−910 ppm). EFs for these RSEs are also elevated during this interval (Mo_{EF} = 14−597, U_{EF} = 7−72, V_{EF} = 2−10).

5.3. Mo isotope compositions at the XJMW section

The 24 samples from the Doushantuo Formation at the XJMW section show mostly positive δ^{98}Mo values, up to +1.82‰ (Fig. 2; Table 1), with only one negative value (−0.39‰) in Member II. Mo isotope compositions are elevated during the three RSE-enriched intervals. In Interval A, two samples from the lowermost Member II have relatively low δ^{98}Mo values (+0.23‰ and +0.37‰, respectively). Between Interval A and Interval B, the δ^{98}Mo data show a limited range except for one negative value. The δ^{98}Mo values increase progressively upsection towards Member IV, with the δ^{98}Mo value showing up to +1.39‰ in Interval B. Moving to Interval C, the δ^{98}Mo values show a range of +0.64 to +1.82‰, averaging +1.29 ± 0.42‰ (1SD). Throughout the XJMW section, the TOC trend generally covaries with the Mo isotopic data. One important finding is that δ^{98}Mo values continue to rise through Member IV (Fig. 2), while the basal Member IV sample has a relatively low δ^{98}Mo value (+0.64‰) and the highest Mo concentration (312 ppm) in the XJMW section.

336 **Table 1.** Geochemical data for Doushantuo Formation at the XJMW section.

Unit	Sample	Height (m)	Age (Ma)	δ^{98}Mo (‰)	TOC (%)	Al (%)	Mo (ppm)	U (ppm)	V (ppm)	Fe_{HR}/Fe_T	Fe_{Py}/Fe_{HR}
Member I	XJMW1	0	635		0.07	7.54	0.3	2.8	66	0.61	0.39
Member I	XJMW2	0.5	634		0.04	3.47	0.4	2.5	43	0.83	0.12
Member I	XJMW3	1.4	633		0.06	1.43	0.9	1.5	13	0.93	0.04
Member II	XJMW4	3	632		0.35	3.06	0.4	7.1	1199	0.88	0.05
Member II	XJMW5	3.6	631		0.05	3.24	1.0	6.2	413	0.94	0.12
Member II	XJMW6	4.6	629	0.234	0.21	8.57	15	14	315	0.77	0.5
Member II	XJMW7	5.6	627	0.368	0.73	7.44	11	7.9	250	0.87	0.44
Member II	XJMW8	6.6	625		0.04	3.63	1.7	5.3	189	0.9	0.24
Member II	XJMW9	8.3	621		0.25	1.46	0.3	3.0	66	0.93	0.07
Member II	XJMW10	9.3	619		0.12	8.76	0.1	6.3	162	0.72	0.6
Member II	XJMW11	11.3	615		0.04	1.38	0.3	0.8	58	0.91	0.11
Member II	XJMW12	12.3	613		0.11	7.42	0.8	1.5	85	0.84	0.75
Member II	XJMW13	14	609		0.09	5.24	0.8	1.2	54	0.81	0.63
Member II	XJMW14	15	607	-0.388	1.69	7.19	1.3	2.2	99	0.88	0.76
Member II	XJMW15	16.4	604		0.13	6.77	0.9	1.6	76	0.52	0.54
Member II	XJMW16	17.4	602	0.672	1.50	7.82	1.2	2.4	95	0.78	0.69
Member II	XJMW17	18.4	600	0.692	0.00	8.03	1.7	2.8	104	0.54	0.44
Member II	XJMW18	20.4	596	0.253	1.33	6.42	2.3	3.5	95	0.85	0.79
Member II	XJMW19	20.8	595		0.80	5.14	2.1	3.0	69	0.91	0.59
Member II	XJMW20	21.1	595	0.434	2.42	7.68	3.6	5.4	105	0.96	0.77
Member II	XJMW21	22.7	591	0.205	1.47	7.17	1.8	3.1	98	0.91	0.78
Member II	XJMW22	22.8	591	0.309		5.26	1.6	1.4	74	0.96	0.76
Member II	XJMW23	23.6	590		0.54	5.14	0.9	2.9	75	0.82	0.72
Member III	XJMW24	24.6	588		0.45	1.94	0.5	1.2	27	0.92	0.38
Member III	XJMW25	26.1	584	0.569	3.45	7.40	9.2	8.8	169	1	0.78
Member III	XJMW26	26.3	584	0.644	2.24	6.86	5.5	6.5	160	0.95	0.85
Member III	XJMW27	26.7	583		0.59	0.74	1.1	0.9	21	0.98	0.26

Member III	XJMW28	27	583	1.386	4.13	5.74	5.6	11	141	0.85	0.81
Member III	XJMW29	27.5	582		2.35	1.88	2.1	1.8	37	0.96	0.45
Member III	XJMW30	27.8	581	1.148	3.05	6.54	11	5.9	106	0.87	0.88
Member III	XJMW31	28.3	580	0.270	0.04	5.46	2.4	3.9	88	0.94	0.78
Member III	XJMW32	29.1	578	0.228	0.33	4.41	2.9	2.3	59	0.94	0.89
Member III	XJMW33	30.1	576		0.05	0.51	0.6	1.7	52		
Member III	XJMW34	30.9	575		0.24	1.82	1.0	3.9	150	0.73	0.51
Member III	XJMW35	31	574		0.11	1.83	0.6	7.8	153	1	0.37
Member III	XJMW36	32.5	571		0.03	2.38	1.1	3.7	397	0.92	0.62
Member IV	XJMW37	33	570	0.640	0.37	6.68	312	48	910	0.89	0.88
Member IV	XJMW38	35	566	1.349	0.09	2.36	6.4	9.2	324	0.99	0.75
Member IV	XJMW39	37	562	0.857	0.30	0.83	94	21	115		
Member IV	XJMW40	37.1	562	1.393	1.54	2.32	34	6.0	128	1	0.85
Member IV	XJMW45	37.2	562	0.805	5.96	2.68	31	21	128	1	0.63
Member IV	XJMW41	37.5	561	1.821	6.19	4.82	66	19	140	0.28	0.77
Member IV	XJMW42	37.65	561	1.722	6.60	5.34	58	19	136	0.99	0.69
Member IV	XJMW43	37.8	560	1.549	7.32	5.07	56	24	140	1	0.71
Member IV	XJMW44	38	560	1.443	7.58	4.86	51	18	133	0.96	0.74

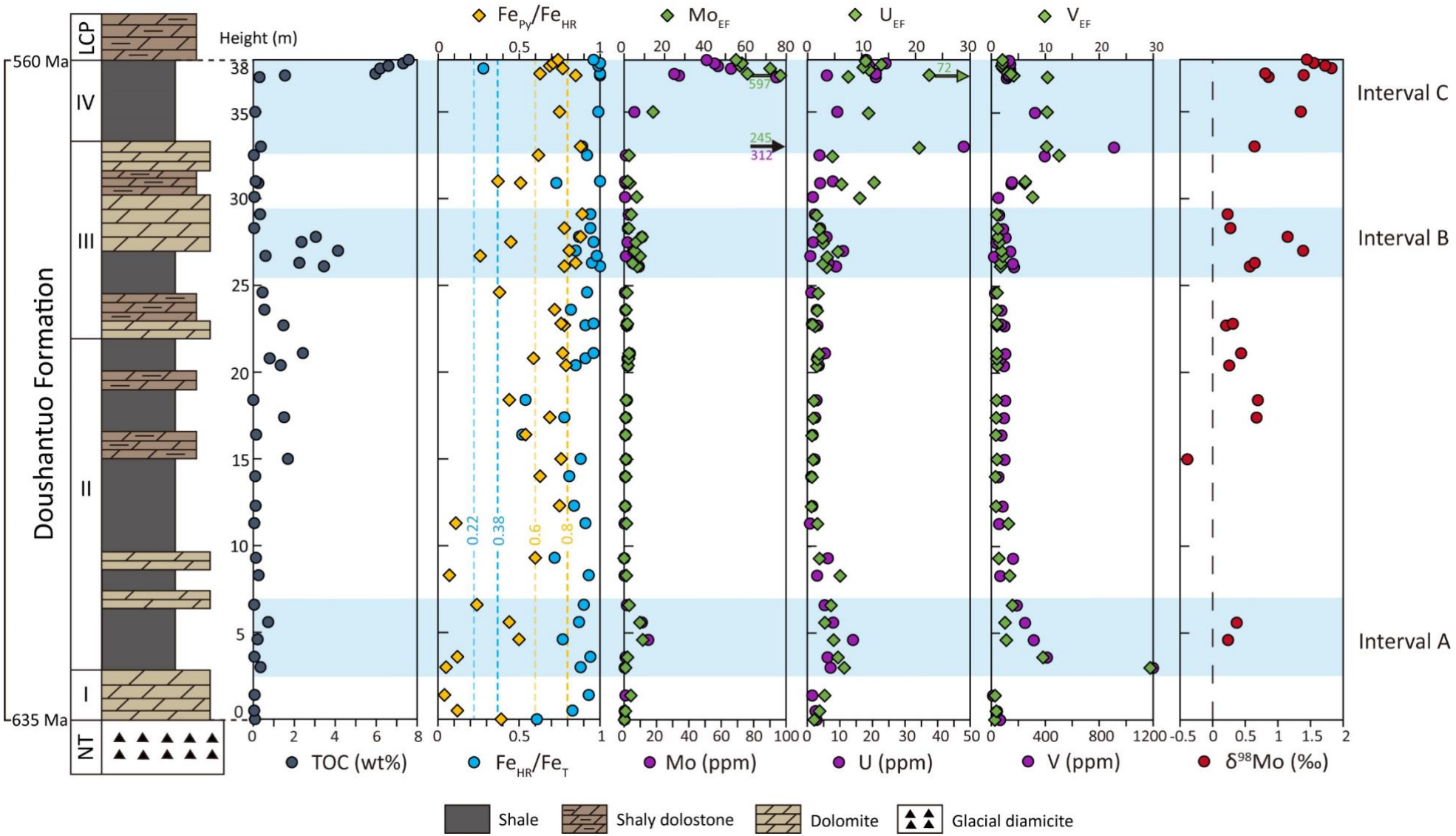
LCP
IV
III
II
I
NT
560 Ma
635 Ma
Doushantuo Formation
Height (m)
Fe$_{Py}$/Fe$_{HR}$
Mo$_{EF}$
U$_{EF}$
V$_{EF}$
0.22
0.38
0.6
0.8
597
72
245
312
Interval C
Interval B
Interval A
TOC (wt%)
Fe$_{HR}$/Fe$_{T}$
Mo (ppm)
U (ppm)
V (ppm)
δ^{98}Mo (‰)
Shale
Shaly dolostone
Dolomite
Glacial diamicite

338

Fig. 2. Geochemical profiles for the XJMW section (Table 1), together with the stratigraphic column. The blue intervals signify high RSE enrichments (roughly RSE_{EF} > 10), Mo isotopic compositions and TOC contents (Interval A, B and C).

6. Discussion

6.1. Three oceanic oxygenation events

Based on our data, three potential oxygenation intervals at the XJMW section (Fig. 2; Interval A: basal Member II, ~630 Ma, Interval B: mid Member III, ~580 Ma, and Interval C: Member IV ~570 Ma) are identified, based on elevated RSE concentrations and enrichment factors, TOC concentrations and δ^{98}Mo values. As mentioned above, the accumulation rates of RSE in reducing environments exceed those in oxic environments (Sahoo, et al., 2012), and with a greater extent of global oxygenation, greater enrichment of RSEs will occur in fewer locally anoxic settings. Therefore, the RSE enrichments of these three episodes suggest widespread OOEs within the investigated late Ediacaran interval. We estimate that each OOE spanned an approximate maximum interval of ~8−10 million years (Table 1), and that dynamic redox variability through the stratigraphy likely regulated sedimentary RSE concentrations. The RSE concentrations shift to lower values between OOEs, which most likely suggests a switch back to more reducing oceanic conditions, in agreement with the interpretation for the Wuhe section by Sahoo et al. (2012, 2016). In general, the timing of these three OOEs generally concurs with that found in previous studies from other slope sections (see Sahoo et al., 2012, 2016;

Kendall et al., 2015; Ostrander et al., 2019; Xu et al., 2022). Based on the Fe speciation data, most samples from the Doushantuo Formation at the XJMW section were deposited under anoxic conditions, which in detail was mostly ferruginous with episodic euxinia. Since Mo, U and V exhibit their own different characteristic responses to redox conditions encountered in the water column and during early diagenesis (Morford et al., 2005), changes in their concentrations during any particular OOE may not necessarily covary (Fig. 2).

In Interval A, a slight [Mo] and [U] increase is observed, despite Fe speciation evidence for ferruginous conditions (Fig. 2). This may reflect changes in the local depositional environment, including openness of the paleo-basin (Algeo and Lyons, 2006) and bulk sedimentation rate (Hardisty et al., 2018). Vanadium shows the highest value at the base of Interval A, while U is only moderately enriched, and Mo is lower than the average upper crustal value. Vanadium enrichment begins under higher Eh conditions (Nielsen, 2020) than U and Mo, and shows high affinity with organic matter, which is consistent with the relatively low Fe_{Py}/Fe_{HR} and high TOC.

In Interval B, Mo concentrations are less than 11 ppm (Fig. 2), and such low concentrations only occur in modern non-euxinic environments where sulphide is restricted to porewaters (Scott and Lyons, 2012). However, Fe_{Py}/Fe_{HR} ratios suggest that redox conditions fluctuated between ferruginous and euxinic conditions (Fig. 2). Therefore, availability of Mo may have been restricted due to a less oxygenated open ocean.

In Interval C, Fe_{Py}/Fe_{HR} data strongly indicate euxinic conditions (Fig. 2), which is similar to Interval B. However, significantly higher RSE concentrations and high TOC contents (>7.5 wt%), with values comparable to those found in Phanerozoic euxinic shales deposited during, or following, periods of global ocean oxygenation (Och and Shields-Zhou, 2012), highlights the potential magnitude of this

particular global OOE.

Samples between OOEs have low Mo_{EF} and U_{EF} values (Fig. 3a), which is consistent with low concentrations of Mo and U in a less oxygenated ocean (Algeo and Tribovillard, 2009). The Mo and U enrichment factors observed in Intervals A and B plot close to, or below, the modern seawater value, but in Interval C range between those for modern open seawater and those for euxinic basins in good connection with the open ocean (Fig. 3a). The high enrichment of RSEs observed in Doushantuo Member IV (Interval C) could have been caused by a local Fe-Mn oxide shuttle and a global-scale OOE (Ostrander et al., 2019).

Furthermore, changes in the degree of connection with the open ocean can also affect Mo abundance in basinal seawater and sediments (Algeo and Lyons, 2006). Due to basin restriction, the modern Black Sea has low deep-water Mo concentrations (~7 nM; Nägler et al., 2011), compared with the modern open ocean (~110 nM; Ho et al., 2018). By analogy, low RSE concentrations from Ediacaran successions in the Yangtze Gorges area are suggested to indicate basin restriction, as the Yangtze Gorges sections were deposited in a proximal intra-shelf lagoon (Jiang et al., 2011; Och et al., 2016). The low RSE concentrations (close to crustal values) between OOEs can only be inferred to be due to a less well-oxygenated global ocean if strong basin restriction can be ruled out. In this context, the XJMW section was located in a distal slope setting which may have been better connected to the open ocean before deposition of Doushantuo Member IV. Therefore, our data may potentially be explained by both oxygenation and basin restriction (see section 6.3). Below we constrain the extent of oxygenation further by exploring Mo isotope systematics.

6.2. Mo isotopes and Mo concentration systematics

405

406 The Mo isotope composition of marine sediments has the potential to record the global extent
407 of euxinia when sequestration of the aqueous molybdate anion, following conversion of molybdate
408 to thiomolybdate species, is near-quantitative. Normally, this process requires relatively high $[H_2S]_{aq}$,
409 low pH (Helz, 2021), and possibly basin restriction (Algeo and Lyons, 2006). Such a combination of
410 conditions may not commonly occur, and so it is commonly assumed that $\delta^{98}Mo$ values of organic
411 rich sediments ($\delta^{98}Mo_{ORS}$) from anoxic basins (e.g., Nanhua Basin) represent a lower estimate for
412 $\delta^{98}Mo_{OSW}$ (Arnold et al., 2004; Neubert et al., 2008). In general, a high, maximal $\delta^{98}Mo_{ORS}$ value, as
413 the estimate for $\delta^{98}Mo_{OSW}$, is taken to reflect a well-oxygenated ocean, while conversely, a low value
414 implies extensive ocean anoxia, especially for sediments deposited under euxinic conditions (Arnold
415 et al., 2004; Kendall et al., 2017). Due to mass balance considerations, $\delta^{98}Mo_{ORS}$ anomalies lower than
416 the crustal composition (~+0.35 to +0.6‰; Willbold and Elliot, 2017) must deviate from $\delta^{98}Mo_{OSW}$.
417 Lower $\delta^{98}Mo_{ORS}$ values than coeval $\delta^{98}Mo_{OSW}$ could be driven by two processes: Fe-Mn (oxyhydr)oxide
418 shuttling (Scholz et al., 2013, 2017) or non-quantitative removal of Mo as thiomolybdate species
419 under weakly sulphidic conditions (Tossell, 2005; Kerl et al., 2017; Hlohowskyj et al., 2021). In this
420 study, the lower $\delta^{98}Mo_{ORS}$ values likely record non-quantitative drawdown of molybdate from the
421 water column, which is supported by lower Fe_{Py}/Fe_{HR} ratios for these samples (Table 1).

422 In the modern ocean, an Fe-Mn oxide shuttle for Mo drawdown has been proposed to operate
423 in open-marine upwelling margins (e.g., California continental borderland, Peruvian margin and
424 Namibian margin) and semi-restricted basins (e.g., Cariaco Basin, Baltic Sea Deeps, and multiple
425 fjords), raising sedimentary Mo_{EF}/U_{EF} ratios above those of seawater (Algeo and Tribovillard, 2009;
426 Goldberg et al., 2012; Scholz et al., 2013, 2017; see Fig. 3). Bulk $\delta^{98}Mo_{ORS}$ values may therefore be

427 controlled by the relative degree to which Fe-Mn (oxyhydr)oxides preferentially adsorb isotopically
428 light Mo (Goldberg et al., 2009; 2012).

429 At the XJMW section, low $\delta^{98}Mo_{ORS}$ values tend to occur between the OOEs for samples where
430 Fe speciation data are in the equivocal zone (Fe_{Py}/Fe_{HR} of 0.6–0.8), but Mo concentrations are low,
431 suggesting a widespread anoxic ocean (Fig. 2). The low $\delta^{98}Mo_{ORS}$ values for the two ferruginous
432 samples in Interval A, lowermost Member II, can only be regarded as lower estimates of $\delta^{98}Mo_{OSW}$,
433 due to probable incomplete conversion of molybdate to tetrathiomolybdate (Goldberg et al., 2009;
434 Brüske et al., 2020). In Interval B, a few euxinic samples (XJMW28 and 30) have higher δ^{98}Mo values
435 but low Mo concentrations (Table 1 and Fig. 2). This may imply relatively expanded ocean oxygenation.
436 Shoaling of the chemocline or regression may have promoted quantitative removal of Mo and
437 minimum Mo isotope fractionation.

438 The highest δ^{98}Mo values (up to +1.8‰) occur in Interval C, Member IV, suggesting widespread
439 ocean oxygenation prior to 560 Ma (Fig. 2). These high δ^{98}Mo values generally co-occur with high RSE
440 concentrations, which is consistent with deposition in a locally euxinic basin connected to an
441 oxygenated global ocean. Interestingly, the sample with the highest Mo and U, and with very high V
442 concentrations at the base of Interval C, has a relatively low δ^{98}Mo value. This could potentially
443 suggest a sudden rise in the size of RSE reservoirs and non-quantitative removal of Mo from coeval
444 seawater as the basin was transitioning to a euxinic state, as shown by the Fe_{Py}/Fe_{HR} data (Fig. 2).
445 After that, all the RSE contents decline dramatically before increasing again as δ^{98}Mo gradually
446 reaches its peak (>+1.8‰), remaining high (~+1.5‰) thereafter.

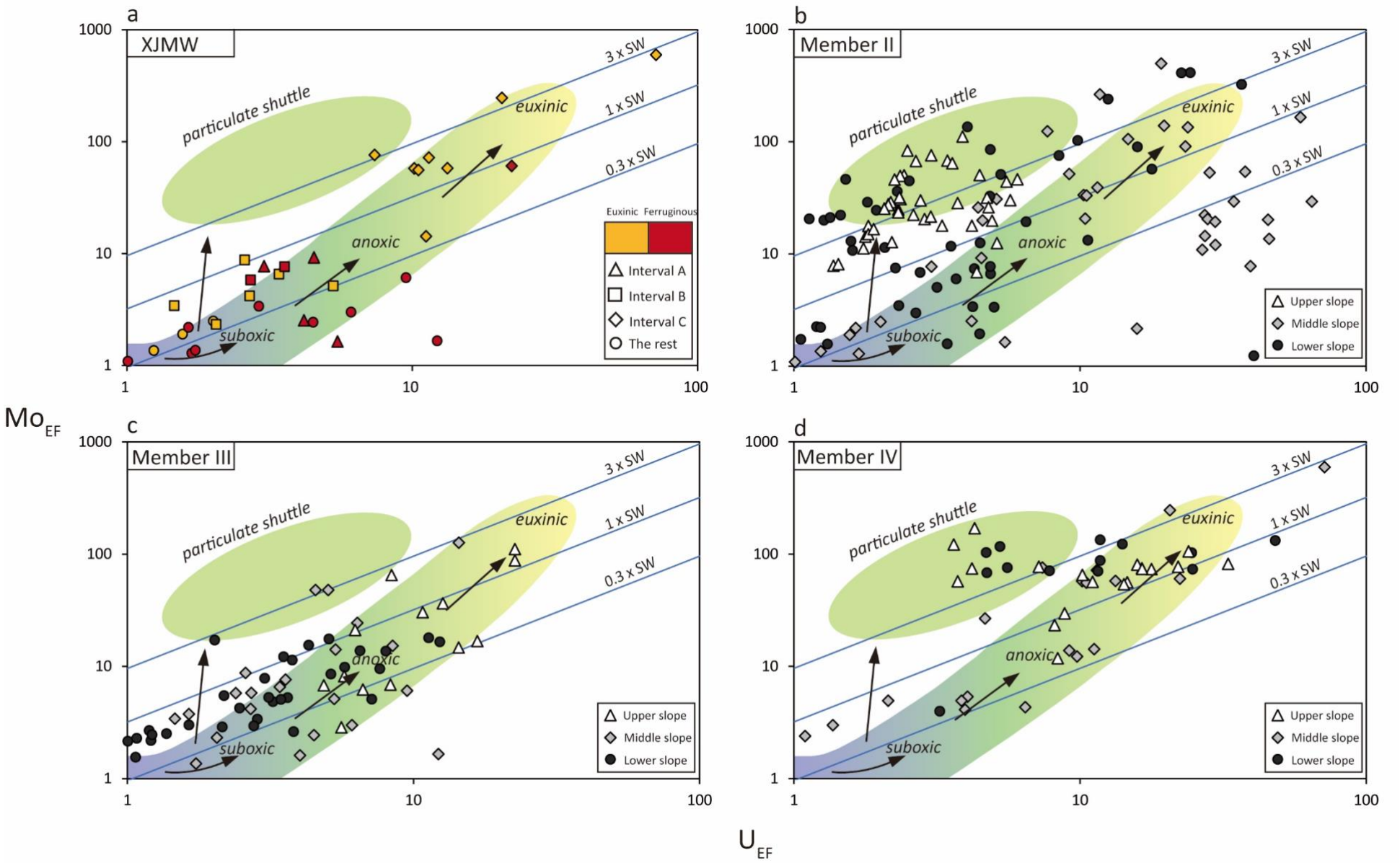
a
XJMW
b
Member II
c
Member III
d
Member IV
particulate shuttle
euxinic
anoxic
suboxic
3 x SW
1 x SW
0.3 x SW
Euxinic Ferruginous
Interval A
Interval B
Interval C
The rest
Upper slope
Middle slope
Lower slope
1000
100
10
1
1
10
100
Mo EF
U EF

447

Fig. 3. (a) Mo_{EF} versus U_{EF} for samples from the XJMW section. (b) (c) (d) Compiled Mo_{EF}/U_{EF} ratios from Doushantuo Members II, III and IV, in slope parts of the Nanhua Basin. Upper slope data include the Rongxi section from Ostrander et al. (2019) and the Daotuo section from Ye et al. (2020). Middle slope data comprise the Taoying section from Ostrander et al. (2019) and the Xiajiaomeng West section from this study. Lower slope data involve the Wuhe and the Yuanjia sections from Ostrander et al. (2019). Solid blue lines are equivalent to multiples of the Mo/U molar ratio of modern seawater (×0.3, ×1, and ×3). Redox condition (suboxic: blue; anoxic: green; euxinic: yellow and arrows show the transitions) and particulate shuttle fields are modified from Algeo and Tribovillard (2009). The "particulate shuttle" is linked to Fe-Mn redox cycling within the water column.

6.3. Implications for Basin Restriction

It has been debated whether the Nanhua Basin maintained a continuous connection with the open ocean during the Ediacaran Period (Sahoo et al., 2012, 2016; Wu et al., 2021; Jin et al., 2021). The study by Ostrander et al. (2019) summarised the use of RSE concentrations and $\delta^{98}Mo$ values as indicators of a non-restricted or restricted basin.

In the modern day, relatively low Mo contents but high $\delta^{98}Mo_{sed}$ values occur in the Black Sea (Neubert et al., 2008) and euxinic basins of Kyllaren fjord (Noordmann et al., 2015), and Lake Rogoznica (Bura-Nakić et al., 2018). These basins capture the coeval $\delta^{98}Mo_{OSW}$, as minimized exchange of Mo from the ocean into these settings promotes near-quantitative removal of Mo to the sediments. As discussed previously, our data from the XJMW section show that the Nanhua Basin was

more likely connected to the open ocean at the time of Member IV deposition, when two major transitions may have occurred. Firstly, the immediate increase in [Mo], [U] and [V] at the start of Member IV deposition may have been caused by transgression or shoaling of the chemocline. Transgression has been proposed by Och et al. (2016), during which a sulphidic wedge was postulated to extend over the platform due to sea-level rise. Secondly, redox conditions in the water column at XJMW changed from equivocal (Fe_{Py}/Fe_{HR} = 0.62) to more demonstrably euxinic (Fe_{Py}/Fe_{HR} = 0.88) (Table 1) at the start of Interval C (prior to the Member III/Member IV boundary), suggesting the probable progressive development of more intense euxinia. This would explain the initial rapid quantitative removal of RSEs from the water column, leading to high RSE values in sample XJMW37 (Table 1). However, this sample has a low δ^{98}Mo value (+0.64‰) suggesting incomplete Mo drawdown from the water column. Immediately above this sample, [Mo] decreases while δ^{98}Mo increases (Fig. 2), suggesting sustained highly euxinic conditions with limited connectivity to the global ocean. This is similar to the modern Black Sea deep water-mass scenario (the "basin reservoir effect"; Tribovillard et al., 2008). Increased and stable [Mo] and [U] at and after sample XJMW39, coupled with high δ^{98}Mo, suggests that at least some connection was regained with the open ocean.

To better understand the basin restriction, we have compiled Mo_{EF}–U_{EF} data from the slope part of the Nanhua Basin. Fig. 3 shows data for slope sections, consisting of our data and published data, interpreted using the Mo_{EF}/U_{EF} model proposed by Algeo and Tribovillard (2009). In general, the consistent covariation in Mo and U enrichment factors between OOEs likely indicates the occurrence of regionally euxinic bottom waters and unrestricted exchange between the local environment and the open ocean during each OOE (Fig. 3a). Member II (Fig. 3b) data show the greatest scatter, with data from the upper slope commonly falling into the particulate shuttle area, consistent with

ferruginous conditions. Apart from a cluster of data from middle-slope sections that indicate some level of possible restriction (some Mo_{EF}/U_{EF} values below 0.3 × SW in the Taoying section), most other sections appear to have been connected to the open ocean, with evidence for euxinia in some of the middle and lower slope sections. Member III (Fig. 3c) data show that a sulphidic wedge moved upslope, appearing in the upper and middle slope sections, with most samples falling in the unrestricted-marine area. For Member IV (Fig. 3d), the majority of data indicate open ocean conditions, with most of the Mo_{EF}/U_{EF} ratios consistently close to or exceeding the 1 × SW line. This is also consistent with the Mo_{EF}–U_{EF} data from intra-shelf sections (Kendall et al., 2015), indicating locally euxinic bottom waters and unrestricted exchange between the local basin and the open ocean (Algeo and Tribovillard, 2009).

Although the basin possibly became semi-restricted during this stage due to the seaward presence of a submerged upland (Yeasmin et al., 2017), similar average Mo/TOC values of Member IV ORM (23 ppm/wt%) to those for the weakly restricted Cariaco Basin (25 ppm/wt%) (Algeo and Lyons 2006; Kendall et al., 2015), as well as high Mo_{EF}/U_{EF} values, suggest that water exchange between the local intra-shelf basin and open ocean was not severely restricted. Mo/TOC data from Member IV at the XJMW section show that high $\delta^{98}Mo$ values only occur when Mo/TOC values are relatively low, indicating that the local basin became progressively more restricted after the deposition of sample XJMW 37 (~570 Ma; Table 1).

6.4. The spatial distribution of Mo data across the Nanhua Basin

The Mo_{EF}/U_{EF} compilation data for slope settings suggest episodic expansion and movement of a

514 euxinic wedge across the slope of the Nanhua Basin. To investigate the spatial extent of redox
515 conditions further, we next present a δ^{98}Mo and [Mo] compilation across the Nanhua Basin. Six
516 sections are placed in a proposed basinal reconstruction of the Nanhua Basin after Lu et al. (2013) in
517 Fig. 4, of which the Jiulongwan section is an intra-shelf section, located in the Yangtze Gorges area
518 (Fig. 1), and the other 5 sections are slope sections discussed above.

519 For Member II (with Interval A at its base), data from the middle-to-lower slope sections (Taoying,
520 Wuhe, and Yuanjia) correlate well (Fig. 4), as these sections were all deposited on the SE-facing slopes
521 of the Nanhua Basin. All three sections evidence greater drawdown of Mo (up to ~180 ppm),
522 indicating euxinic bottom waters. By contrast, the upper and middle slope sections (Rongxi and XJMW)
523 have only slightly elevated [Mo]. Similarly, published Mo concentrations for Member II on the Yangtze
524 platform are not particularly high (Och et al. 2016; Zhu et al. 2018). The Fe speciation data for slope
525 sections show variations between oxic, ferruginous and euxinic bottom waters (Sahoo et al., 2012,
526 2016; Ostrander et al., 2019). A few samples at the Yuanjia section have high δ^{98}Mo values and [Mo],
527 which may be due to highly sulphidic conditions in this area. Negative δ^{98}Mo excursions with high Mo
528 concentrations found in these deeper sections may have been the result of a deepening of the local
529 chemocline, resulting in the establishment of an Fe-Mn oxide shuttle and drawdown of Mo to the
530 sediments (Ostrander et al., 2019). This effect, being particularly pronounced during OOEs, suggests
531 fluctuations between oxic and euxinic bottom waters (Ostrander et al., 2019). However, the most
532 negative δ^{98}Mo values in Member II at the Taoying section co-occur with low [Mo], which may be due
533 to a large negative Mo isotope fractionation under weakly sulphidic conditions.

534 For Member III (Interval B), only limited data exist for these sections, likely due to its carbonate-
535 rich lithology. A similar pattern of δ^{98}Mo evolution is observed in the middle slope XJMW and Taoying

sections, but the possibly deeper Wuhe section has more negative δ^{98}Mo values. High δ^{98}Mo values (XJMW section: up to ~+1.4‰) and high Mo concentrations (Taoying section: up to 76 ppm) are found in the middle slope of the basin. However, as carbonate is a relatively untested and potentially ambiguous material for Mo isotope study (Kendall, et al., 2017), alternative proxies are needed. The δ^{238}U data (around −0.2‰) of carbonate from different cratons, including the South China craton, suggest a global oceanic oxygenation event (Zhang et al., 2019).

For Member IV (Interval C), the Jiulongwan, Rongxi and Wuhe sections start with negative δ^{98}Mo values and high Mo concentrations in the lower part, but near modern seawater δ^{98}Mo values higher in the section. The XJMW section does not exhibit negative δ^{98}Mo values, but follows a similar trend to those sections. The Taoying section has very low [Mo] and only one reported δ^{98}Mo value, as samples were all deposited under ferruginous conditions. At Wuhe section, the samples with high Mo concentrations mostly have negative δ^{98}Mo values. Some studies proposed that the late Ediacaran marine redox state was highly heterogeneous (Li et al., 2015; Och et al., 2016), accompanied by negative δ^{98}Mo values and substantial enrichment in Mo at the Yangtze Gorges sections (Kendall et al., 2015). We suggest that the bottom waters in the intra-shelf basin at the start of Member IV deposition (Jiulongwan: [Mo] = 663 ppm) were euxinic, and that a euxinic wedge extended to the outer slopes (Rongxi: [Mo] = 95 ppm and XJMW: [Mo] = 312 ppm). As the rapid increase of [Mo] occurs at the base of Member IV in intra shelf, upper, middle and lower slope portions of the basin, transgression (maximum flooding of the Shuram transgression; Busch et al., 2022) likely occurred at the beginning of Doushantuo Member IV deposition (~570 Ma). The accompanying deepening of the chemocline may have supplied an extra source of light Mo isotopes through reductive dissolution of Fe-Mn oxides (Ostrander et al., 2019).

At the top of Member IV, the Jiulongwan section on the Yangtze platform retains relatively high Mo concentrations (>100 ppm), and δ^{98}Mo exceeds 2‰ (Fig. 4). A peak in δ^{98}Mo values can be correlated with the upper slope sections, Rongxi (~+1.3‰) and XJMW (~+1.8‰), with all [Mo] higher than 20 ppm (Interval C; Fig. 4). The Fe_{Py}/Fe_{HR} ratios of Jiulongwan Member IV are all above 0.8 (Kendall et al., 2015), while ratios fluctuate at Rongxi and XJMW. This suggests that the Jiulongwan section records δ^{98}Mo closest to that of the late Ediacaran open ocean. The maximum value for this section (+2‰) is close to modern seawater (~+2.34‰), indicating widespread global ocean oxygenation, which is also supported by the mean δ^{238}U value of 0.24 ± 0.16‰ for the ORM from Member IV in the Yangtze Gorges region (Kendall et al. 2015).

Overall, our data and the compiled data suggest that the redox evolution of the Nanhua Basin can be summarized as follows: Interval A in Member II portrays a partially restricted basin with euxinic bottom water and RSE enrichments, indicating global oceanic oxygenation; Interval B in Member III presents a euxinic wedge on the mid-slope, with higher δ^{98}Mo (~+1.4‰) at XJMW and δ^{238}U values indicating oxygenation; Member IV (Interval C) is characterized by euxinic bottom waters in the intra-shelf basin, fluctuating euxinia on upper to mid-slopes, with later peak δ^{98}Mo (~+2‰) and δ^{238}U values indicating global oceanic oxygenation close to modern ocean levels.

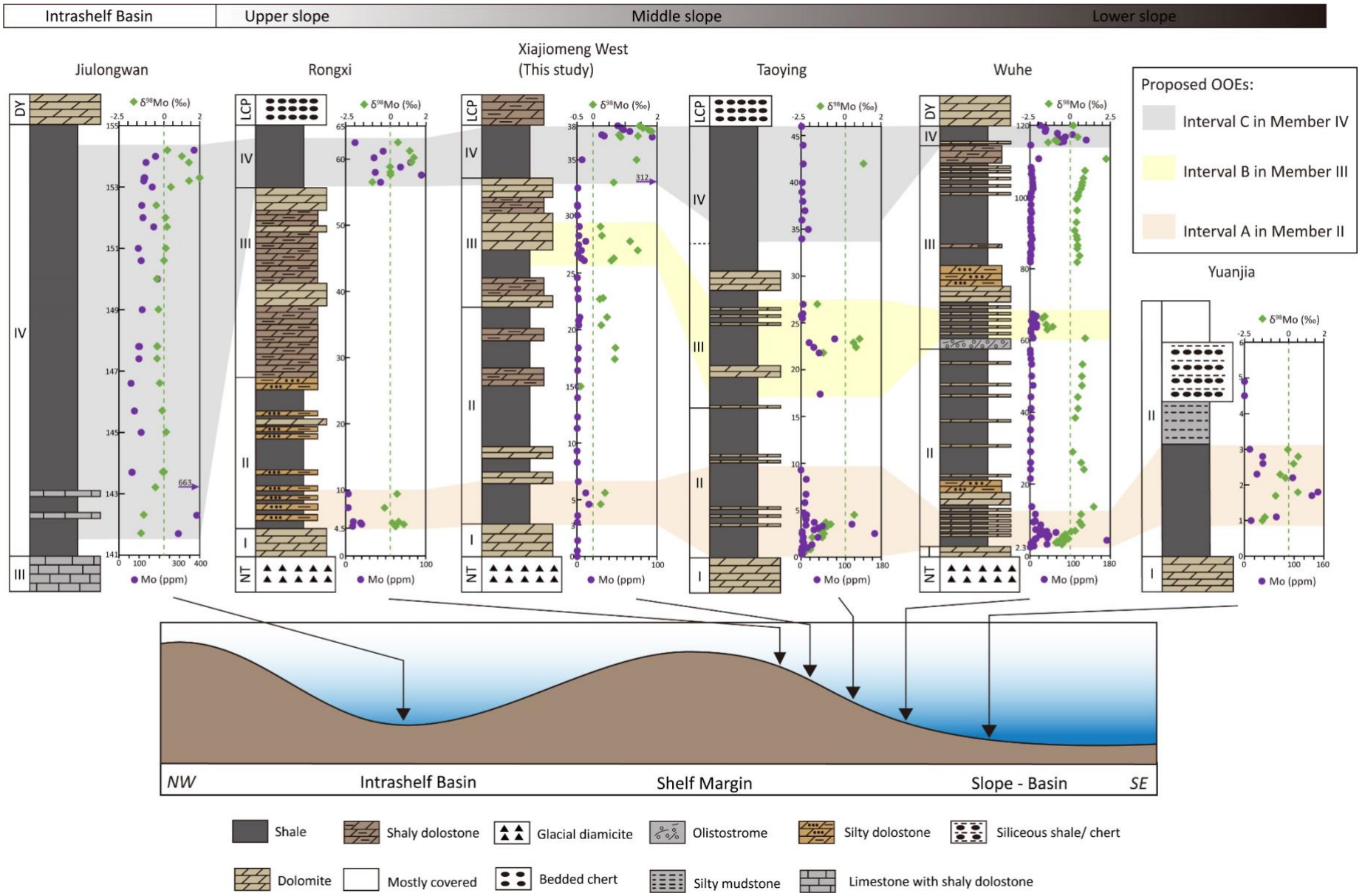
Intrashelf Basin
Upper slope
Middle slope
Lower slope
Jiulongwan
Rongxi
Xiajiomeng West
(This study)
Taoying
Wuhe
Yuanjia
δ98Mo (‰)
Mo (ppm)
Proposed OOEs:
Interval C in Member IV
Interval B in Member III
Interval A in Member II
NW
Intrashelf Basin
Shelf Margin
Slope - Basin
SE
Shale
Shaly dolostone
Glacial diamicite
Olistostrome
Silty dolostone
Siliceous shale/ chert
Dolomite
Mostly covered
Bedded chert
Silty mudstone
Limestone with shaly dolostone

574

Fig. 4. The spatial distribution of Mo data across the Nanhua Basin together with litho-stratigraphic logs. The bottom figure shows the basinal reconstruction of the Yangtze Platform (cross-section view). The data for the Jiulongwan section are from Kendall et al. (2015). The XJMW section data are from this study. Rongxi, Taoying, Yuanjia and Wuhe section data are from Sahoo et al. (2012, 2016) and Ostrander et al. (2019). The lithological logs of these sections are based on the descriptions in the mentioned papers. Intervals A, B, and C indicate the proposed OOEs.

6.5. Temporal trends in ocean oxygenation: A molybdenum perspective

To place our data in a broader context, we compiled δ^{98}Mo and [Mo] data from the Ediacaran to early Cambrian, which includes data mainly from South China, Canada, and Czech Republic (Fig. 5). Between 635 Ma and ~620 Ma, Mo concentrations exhibit a spike (>170 ppm), with δ^{98}Mo values showing large variations (from −2.24 to +1.47‰). This may document the earliest widespread ocean oxygenation in the wake of the Marinoan glaciation (Sahoo et al., 2012). The negative δ^{98}Mo data are all from the lower Member II of the Doushantuo Formation at different sections (Ostrander et al., 2019). As explained above, the very negative δ^{98}Mo values with relatively high Mo concentrations may have been the result of changes in the position of the local chemocline and in global sea level (Ostrander et al., 2019). It is possible that during this time, ocean oxygenation was enhanced locally, stimulating operation of the Fe-Mn oxide Mo shuttle.

Following the first OOE occurrence, an interval of generally variable δ^{98}Mo and low Mo concentrations (close to crustal value, 2–4 ppm) between ~620 Ma and ~580 Ma possibly indicates a return to a small oceanic Mo reservoir, with most samples deposited under variable local redox

conditions (mainly ferruginous), as indicated by published Fe speciation data (Johnston et al., 2013). As previously discussed for the OOEs in our section, at ~580 Ma (Interval B; Fig. 2), δ^{98}Mo values exceeded the river input value (+0.7‰), and Mo concentrations show modest enrichment, which is also consistent with Chen et al. (2015). Sahoo et al. (2016) compiled other RSE (U, V, Re and Cr) data that all show substantial enrichment at this time.

In the late Ediacaran, between ~570 Ma and ~560 Ma, δ^{98}Mo values reach >+2‰ (approaching modern seawater) for the first time in Earth's history, and Mo concentrations rise to the highest value (>600 ppm) (Fig. 5), as recorded for the Member III/Member IV boundary at Wuhe section (Ostrander et al., 2019) and Member IV at Jiulongwan section (Kendall et al., 2015). The sudden rise in [Mo] indicates that the Shuram excursion may have coincided with an increase in the size of the oceanic Mo reservoir, which is also consistent with the rise in sulphate reservoir during this time (Shi et al., 2018). Our data from the XJMW section confirm the δ^{98}Mo spike in Member IV, and Mo enrichment is significant (>300 ppm) throughout Member IV, which indicates a pulse of ocean oxygenation close to modern levels in the late Ediacaran.

Generally, these late Ediacaran OOEs may help explain the diversification of multicellular organisms, especially animals. The first appearance of the soft-bodied deep-water Ediacaran macrobiota in Newfoundland, now dated to between 574 and 564 Ma (Matthews et al., 2021), can be linked with a deep-ocean oxygenation event after ~580 Ma (Canfield et al., 2007). The global OOE recorded by Doushantuo Member IV black shale is coincident with the appearance of the Wenghui biota, the Miaohe biota, and the White Sea assemblage between ~570 Ma and 550 Ma (Zhang et al., 2019; Rooney et al., 2020; Yang et al., 2021). The more diversified shallow-water Ediacaran assemblages, including the earliest bilaterians and calcifiers, appeared between 558 Ma and 539 Ma

(Bengtson and Zhao, 1992; Narbonne et al., 2009; Johnston et al., 2012; Warren et al., 2012; Xiao et al., 2021). All of these Ediacaran biota appeared above Interval B, which is consistent with generally more expansive oxygenation indicated by the compiled Mo data. It is therefore likely that the OOEs played an important role in stimulating and accelerating the diversification of metazoans, as more complex food webs and larger animals require higher oxygen levels (Knoll and Carroll, 1999).

In terms of how the OOEs came about, it has been suggested that these oxygenation events were driven by high nutrient input from increased terrestrial weathering (Lyons et al., 2014). Major transgressions happened at least twice during Doushantuo Formation deposition (Member I, and Member III to IV) as mentioned before, potentially bringing more nutrients into the Ediacaran ocean. Furthermore, the study by Shields et al. (2019) proposed that pyrite burial drove Ediacaran oxygenations, sustained by an elevated nutrient flux and the weathering of evaporite sulphate minerals. Neoproterozoic seawater $^{87}Sr/^{86}Sr$ isotope also shows a peak (~0.7087) at ~560 Ma (Cox et al., 2016; Zhou et al., 2020; Chen et al., 2022), indicating increased weathering input, which is consistent with these and other suggestions of a nutrient driver for both the oxygenation events and coeval biotic radiations.

However, this increase in Mo values was not unidirectional. A return to less oxygenated deep ocean conditions from ~550 Ma to ~530 Ma is marked by lower $\delta^{98}Mo$ values and Mo concentrations (Fig. 5), although the occurrence of OOEs became more frequent after the end of the Ediacaran Period, based on Mo enrichments (~540 Ma, ~530 Ma, and ~520 Ma). At ~521 Ma, $\delta^{98}Mo$ reached modern seawater values of ~+2.3‰ in multiple South China sections, corresponding to widespread ocean oxygenation, likely triggering radiations of aerobic bilaterians (Chen et al., 2015).

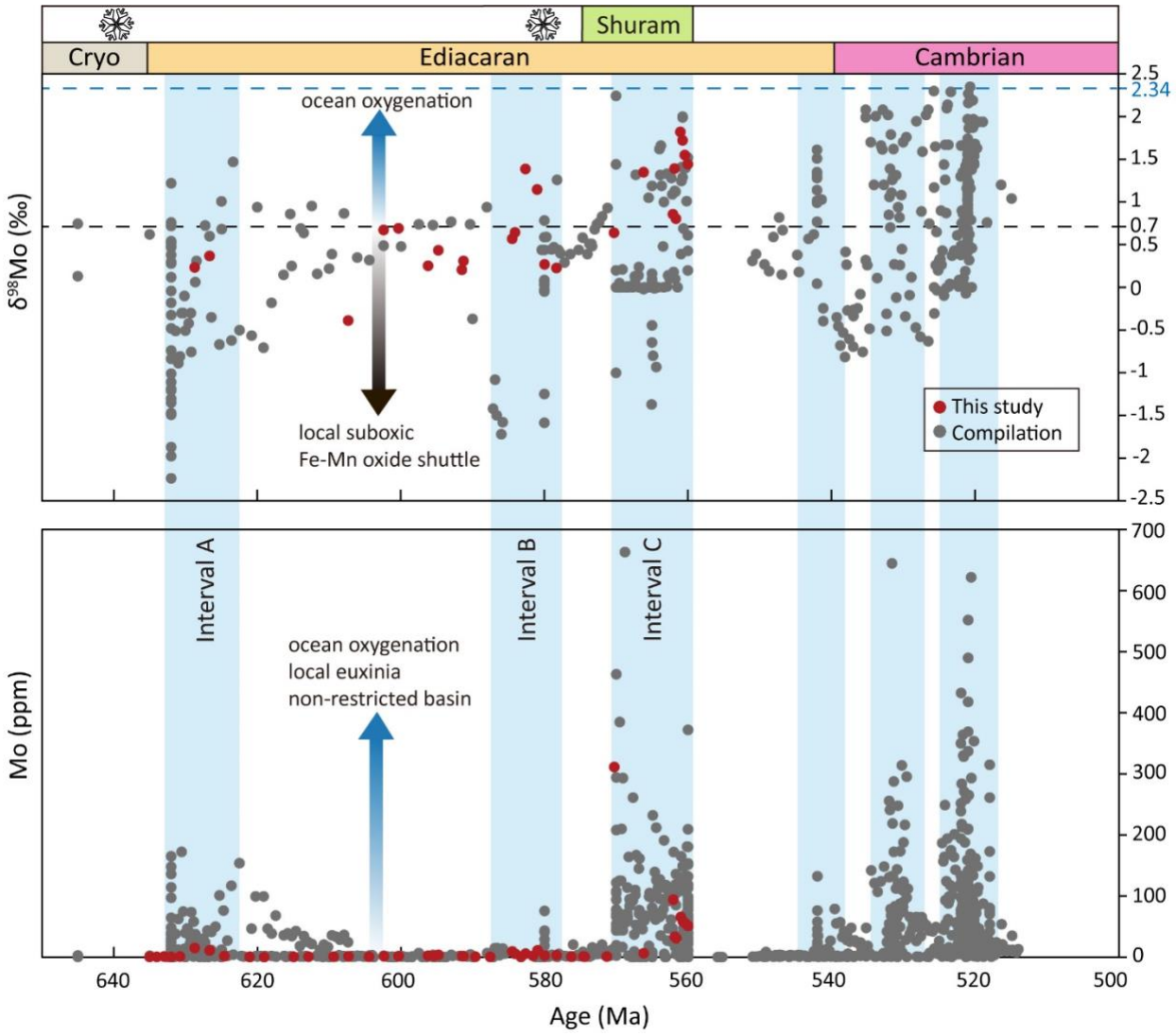

Fig. 5. A temporal record of δ^{98}Mo and [Mo] based on this study and published data. Blue intervals indicate the three OOEs that occurred during the Ediacaran to Cambrian periods. In the time scale, the two snowflakes mark the major glaciations (Marinoan and Gaskiers). 'This study' indicates the newly obtained data from the XJMW section. 'Compilation' refers to updated Mo data compilation after Chen et al. (2015) and additional data source include Wen et al., 2015; Kendall et al., 2015; Kurzweil et al., 2015; Cheng et al., 2017; Sahoo et al., 2016; Zhu et al., 2018; Ostrander et al., 2019; Ye et al., 2020. The age model has been updated based Rooney et al. (2020), Yang et al. (2021), Bowyer et al. (2022) and a constant sedimentation rate model is used to calculate the ages of compiled data.

Two dashed lines mark the average modern seawater δ^{98}Mo value (+2.34‰) and the riverine input (+0.7‰).

7. Conclusions

In order to explore oxygenation events and redox conditions in the Ediacaran ocean, we measured redox-sensitive element (RSE) abundances and Mo isotope compositions for the Doushantuo Formation at the Xiajiaomeng West (XJMW) section on the Nanhua Basin slope. By comparing these new data to previously published data, our main findings are as follows:

1) Our data from the newly discovered XJMW section shows that three OOEs occurred during the Ediacaran Period (~630 Ma, ~580 Ma and ~570 Ma), on the basis of high RSE concentrations paired with elevated δ^{98}Mo values. Importantly, the last OOE points to an extensively oxygenated ocean at ~570 Ma. The findings are generally consistent with other RSE studies (e.g., Scott et al., 2008; Sahoo et al., 2016), and is supported by U isotope data from South China, Siberia, USA (Zhang et al., 2019) and Namibia (Tostevin et al., 2019), and by Cr isotope data from the Wuhe section (Xu et al., 2022). The low RSE concentrations (close to crustal values) between OOEs indicate periodic re-development of extensive ocean anoxia.

2) The Nanhua Basin generally had a good connection to the open ocean. Two transgressions (Member I, and Member III to IV) are supported by our compiled data (Figs. 4 and 5). However, the Yangtze Gorges area may have gradually become more restricted, with limited connection to the open ocean, due to possible regression towards the end of Member IV deposition. This may explain a decrease in RSE concentrations coupled with higher δ^{98}Mo values. Additionally, shoaling of the chemocline could be another possible interpretation.

3) Fe speciation data indicate that almost all of the Doushantuo Formation was deposited beneath an anoxic water column, fluctuating between ferruginous and euxinic conditions. Most Member

675 IV samples were deposited under euxinic conditions, with some indication of a transient oxic
676 episode.

677 4) A compilation of δ^{98}Mo and [Mo] data reveals that ocean oxygenation waxed and waned during
678 the late Neoproterozoic. Our new data and updated compilation show that δ^{98}Mo values
679 approached the modern value at around ~570 Ma, pointing to a widespread oxygenated ocean
680 at that time. The three proposed OOEs occurred in otherwise anoxic Ediacaran oceans, with
681 dynamically shifting euxinic wedges on the slopes of the Nanhua Basin evidenced from a spatial
682 comparison between different sections. The increased frequency of OOEs after the end of the
683 Ediacaran Period (~540 Ma, ~530 Ma, and ~520 Ma) may have stimulated biotic innovations and
684 radiations.

CRediT authorship contribution statement

Lin Yuan: Investigation, Writing - Original Draft, Writing - Review & Editing, Visualization. **Ying Zhou:** Conceptualization, Methodology, Investigation, Resources, Writing - Review & Editing, Funding acquisition, Supervision. **Xi Chen:** Methodology, Resources, Writing - Review & Editing, Supervision. **Maoyan Zhu:** Resources, Writing - Review & Editing, Funding acquisition. **Simon W. Poulton:** Writing - Review & Editing. **Zheyu Tian:** Investigation. **Da Li:** Investigation. **Matthew Thirlwall:** Investigation. **Graham A. Shields:** Resources, Writing - Review & Editing, Funding acquisition.

Declaration of Competing Interest

The authors declare that they have no known competing financial interests or personal relationships that could have appeared to influence the work reported in this paper.

Acknowledgements

We are grateful to Gary Tarbuck (UCL), Andy Hobson (Leeds) and Stephen Reid (Leeds) for technical support in the labs. This study was financially supported by the joint NERC-NSFC Biosphere Evolution Transitions and Resilience (BETR) programme (NE/P01643/1, NSFC/41661134048), the NERC project North China craton: A unique window into Earth's middle age (NE/R010129/1) and the

Strategic Priority Research Program (B) of the Chinese Academy of Sciences (XDB26000000). Constructive comments by Swapan Sahoo and an anonymous reviewer improved the manuscript significantly. And we also thank Jian Zhang and Frances Westall for their editorial handling.

Appendix A. Supplementary Material

Supplementary data to this article can be found online at…

References

Acquisti C., Kleffe J. and Collins S. (2006) Oxygen content of transmembrane proteins over macroevolutionary time scales. Nature 445, 47–52.

Alcott L. J., Krause A. J., Hammarlund E. U., Bjerrum C. J., Scholz F., Xiong Y., Hobson A. J., Neve L., Mills B. J. W., März C., Schnetger B., Bekker A. and Poulton S. W. (2020) Development of Iron Speciation Reference Materials for Palaeoredox Analysis. Geostand. Geoanal. Res. 44, 581–591.

Algeo T. J. and Lyons T. W. (2006) Mo–total organic carbon covariation in modern anoxic marine environments: Implications for analysis of paleoredox and paleohydrographic conditions. Paleoceanography 21, PA1016.

Algeo T. J. and Maynard J. B. (2004) Trace-element behavior and redox facies in core shales of Upper Pennsylvanian Kansas-type cyclothems. Chem. Geol. 206, 289–318.

Algeo T. J. and Tribovillard N. (2009) Environmental analysis of paleoceanographic systems based on molybdenum–uranium covariation. Chem. Geol. 268, 211–225.

Anbar A. D. (2004) Molybdenum Stable Isotopes: Observations, Interpretations and Directions. Rev. Mineral. Geochem. 55, 429–454.

Anderson T. F. and Raiswell R. (2004) Sources and mechanisms for the enrichment of highly reactive iron in euxinic Black Sea sediments. Am. J. Sci. 304, 203–233.

Archer C. and Vance D. (2008) The isotopic signature of the global riverine molybdenum flux and anoxia in the ancient oceans. Nature Geoscience 1, 597–600.

Arnold G. L., Anbar A. D., Barling J. and Lyons T. W. (2004) Molybdenum Isotope Evidence for Widespread Anoxia in Mid-Proterozoic Oceans. Science 304, 87–90.

Barling J., Arnold G. L. and Anbar A. D. (2001) Natural mass-dependent variations in the isotopic composition of molybdenum. Earth Planet. Sci. Lett. 193, 447–457.

Bengtson S. and Zhao Y. (1992) Predatorial Borings in Late Precambrian Mineralized Exoskeletons. Science 257, 367–369.

Benkovitz A., Matthews A., Teutsch N., Poulton S. W., Bar-Matthews M. and Almogi-Labin A. (2020) Tracing water column euxinia in Eastern Mediterranean Sapropels S5 and S7. Chem. Geol. 545, 119627.

Bowyer F. T., Zhuravlev A. Y., Wood R., Shields G. A., Zhou Y., Curtis A., Poulton S. W., Condon D. J., Yang C. and Zhu M. (2022) Calibrating the temporal and spatial dynamics of the Ediacaran - Cambrian radiation of animals. Earth Sci. Rev. 225, 103913.

Bowyer F., Wood R. A. and Poulton S. W. (2017) Controls on the evolution of Ediacaran metazoan ecosystems: A redox perspective. Geobiology 15, 516–551.

Breit G. N. and Wanty R. B. (1991) Vanadium accumulation in carbonaceous rocks: A review of geochemical controls during deposition and diagenesis. Chem. Geol. 91, 83–97.

Bristow T. F. and Kennedy M. J. (2008) Carbon isotope excursions and the oxidant budget of the Ediacaran atmosphere and ocean. Geology 36, 863–866.

Brüske A., Weyer S., Zhao M. Y., Planavsky N. J., Wegwerth A., Neubert N., Dellwig O., Lau K. v. and Lyons T. W. (2020) Correlated molybdenum and uranium isotope signatures in modern anoxic sediments: Implications for their use as paleo-redox proxy. Geochim. Cosmochim. Acta 270, 449–474.

Bura-Nakić E., Andersen M. B., Archer C., de Souza G. F., Marguš M. and Vance D. (2018) Coupled Mo-U abundances and isotopes in a small marine euxinic basin: Constraints on processes in euxinic basins. Geochim. Cosmochim. Acta 222, 212–229.

Busch J. F., Hodgin E. B., Ahm A. S. C., Husson J. M., Macdonald F. A., Bergmann K. D., Higgins J. A. and Strauss J. v. (2022) Global and local drivers of the Ediacaran Shuram carbon isotope excursion. Earth Planet. Sci. Lett. 579, 117368.

Cai Y., Hua H., Xiao S., Schiffbauer J. D. and Li P. (2010) Biostratinomy of the late Ediacaran pyritized Gaojiashan lagerstatte from southern Shaanxi, south China: importance of event deposits. Palaios 25, 487–506.

Calver C. R. (2000) Isotope stratigraphy of the Ediacarian (Neoproterozoic III) of the Adelaide Rift Complex, Australia, and the overprint of water column stratification. Precambrian Res. 100, 121–150.

Calver C. R., Crowley J. L., Wingate M. T. D., Evans D. A. D., Raub T. D. and Schmitz M. D. (2013) Globally synchronous Marinoan deglaciation indicated by U-Pb geochronology of the Cottons Breccia, Tasmania, Australia. Geology 41, 1127–1130.

Canfield, D.E. (2005) The early history of atmospheric oxygen: homage to Robert M. Garrels. Annu. Rev. Earth Planet. Sci. 33, 1–36.

Canfield D. E., Poulton S. W., Knol A. H., Narbonne G. M., Ross G., Goldberg T. and Strauss H. (2008) Ferruginous conditions dominated later neoproterozoic deep-water chemistry. Science 321, 949–952.

Canfield D. E., Poulton S. W. and Narbonne G. M. (2007) Late-Neoproterozoic deep-ocean oxygenation and the rise of animal life. Science 315, 92–95.

Canfield D. E., Raiswell R., Westrich J. T., Reaves C. M. and Berner R. A. (1986) The use of chromium reduction in the analysis of reduced inorganic sulfur in sediments and shales. Chem. Geol. 54, 149–

155.

Chen X., Ling H. F., Vance D., Shields-Zhou G. A., Zhu M., Poulton S. W., Och L. M., Jiang S. Y., Li D., Cremonese L. and Archer C. (2015) Rise to modern levels of ocean oxygenation coincided with the Cambrian radiation of animals. Nature Communications 6, 1–7.

Chen, X., Zhou, Y. and Shields, G.A. (2022) Progress towards an improved Precambrian seawater 87Sr/86Sr curve. Earth Sci. Rev. 224, 103869.

Chen Z., Zhou C., Xiao S., Wang W., Guan C., Hua H. and Yuan X. (2014) New Ediacara fossils preserved in marine limestone and their ecological implications. Scientific Reports 4, 1–10.

Cheng M., Li C., Zhou L., Feng L. J., Algeo T. J., Zhang F. F., Romaniello S., Jin C. S., Ling H. F. and Jiang S. Y. (2017) Transient deep-water oxygenation in the early Cambrian Nanhua Basin, South China. Geochim. Cosmochim. Acta 210, 42–58.

Clarkson M. O., Poulton S. W., Guilbaud R. and Wood R. A. (2014) Assessing the utility of Fe/Al and Fe-speciation to record water column redox conditions in carbonate-rich sediments. Chem. Geol. 382, 111–122.

Cole D. B., Mills D. B., Erwin D. H., Sperling E. A., Porter S. M., Reinhard C. T. and Planavsky N. J. (2020) On the co-evolution of surface oxygen levels and animals. Geobiology 18, 260–281.

Condon D., Zhu M., Bowring S., Wang W., Yang A. and Jin Y. (2005) U-Pb ages from the neoproterozoic Doushantuo Formation, China. Science 308, 95–98.

Cox, G.M., Halverson, G.P., Stevenson, R.K., Vokaty, M., Poirier, A., Kunzmann, M., Li, Z.X., Denyszyn, S.W., Strauss, J.V. and Macdonald, F.A. (2016) Continental flood basalt weathering as a trigger for Neoproterozoic Snowball Earth. Earth Planet. Sci. Lett. 446, 89–99.

Dahl T. W., Hammarlund E. U., Anbar A. D., Bond D. P. G., Gill B. C., Gordon G. W., Knoll A. H., Nielsen A. T., Schovsbo N. H. and Canfield D. E. (2010) Devonian rise in atmospheric oxygen correlated to the radiations of terrestrial plants and large predatory fish. Proc. Natl. Acad. Sci. 107, 17911–17915.

Dickson A. J., Cohen A. S. and Coe A. L. (2012) Seawater oxygenation during the Paleocene-Eocene Thermal Maximum. Geology 40, 639–642.

Dickson A. J., Jenkyns H. C., Idiz E., Sweere T. C., Murphy M. J., van den Boorn S. H. J. M., Ruhl M., Eldrett J. S. and Porcelli D. (2021) New Constraints on Global Geochemical Cycling During Oceanic Anoxic Event 2 (Late Cretaceous) From a 6-Million-year Long Molybdenum-Isotope Record. Geochem. Geophys. Geosyst. 22, e2020GC009246.

Droser, M.L., Tarhan, L.G. and Gehling, J.G. (2017) The rise of animals in a changing environment: global ecological innovation in the late Ediacaran. Annu. Rev. Earth Planet. Sci. 45, 593-617.

Dunk R. M., Mills R. A. and Jenkins W. J. (2002) A reevaluation of the oceanic uranium budget for the Holocene. Chem. Geol. 190, 45–67.

Erickson B.E., Helz G.R. (2000) Molybdenum (VI) speciation in sulfidic waters: stability and lability of thiomolybdates. Geochim. Cosmochim. Acta 64, 1149–1158.

Fike D. A., Grotzinger J. P., Pratt L. M. and Summons R. E. (2006) Oxidation of the Ediacaran Ocean. Nature 444, 744–747.

Frei R., Gaucher C., Poulton S. W. and Canfield D. E. (2009) Fluctuations in Precambrian atmospheric oxygenation recorded by chromium isotopes. Nature 461, 250–253.

Goldberg T., Archer C., Vance D. and Poulton S. W. (2009) Mo isotope fractionation during adsorption to Fe (oxyhydr)oxides. Geochim. Cosmochim. Acta 73, 6502–6516.

Goldberg T., Archer C., Vance D., Thamdrup B., McAnena A. and Poulton S. W. (2012) Controls on Mo isotope fractionations in a Mn-rich anoxic marine sediment, Gullmar Fjord, Sweden. Chem. Geol. 296–297, 73–82.

Goldberg T., Poulton S. W., Wagner T., Kolonic S. F. and Rehkämper M. (2016) Molybdenum drawdown during Cretaceous Oceanic Anoxic Event 2. Earth Planet. Sci. Lett. 440, 81–91.

Hardisty D. S., Lyons T. W., Riedinger N., Isson T. T., Owens J. D., Aller R. C., Rye D. M., Planavsky N. J., Reinhard C. T., Gill B. C., Masterson A. L., Asael D. and Johnston D. T. (2018) An evaluation of sedimentary molybdenum and iron as proxies for pore fluid paleoredox conditions. Am. J. Sci. 318, 527–556.

Helz, G.R. (2021) Dissolved molybdenum asymptotes in sulfidic waters. Geochem. Perspect. Lett. 19, 23–26.

Helz G. R., Miller C. v., Charnock J. M., Mosselmans J. F. W., Pattrick R. A. D., Garner C. D. and Vaughan D. J. (1996) Mechanism of molybdenum removal from the sea and its concentration in black shales: EXAFS evidence. Geochim. Cosmochim. Acta 60, 3631–3642.

Hlohowskyj S. R., Chen X., Romaniello S. J., Vorlicek T. P., Anbar A. D., Lyons T. W. and Chappaz A. (2021) Quantifying Molybdenum Isotopic Speciation in Sulfidic Water: Implications for the Paleoredox Proxy. ACS Earth Space Chem. 5, 2891–2899.

Ho P., Lee J. M., Heller M. I., Lam P. J. and Shiller A. M. (2018) The distribution of dissolved and particulate Mo and V along the U.S. GEOTRACES East Pacific Zonal Transect (GP16): The roles of oxides and biogenic particles in their distributions in the oxygen deficient zone and the hydrothermal plume. Mar. Chem. 201, 242–255.

Holland H. D. (2002) Volcanic gases, black smokers, and the great oxidation event. Geochim. Cosmochim. Acta 66, 3811–3826.

Jiang G., Shi X., Zhang S., Wang Y. and Xiao S. (2011) Stratigraphy and paleogeography of the Ediacaran Doushantuo Formation (ca. 635–551 Ma) in South China. Gondwana Res. 19, 831–849.

Jin C., Li C., Algeo T. J., Wang G., Shi W., Cheng M., Zhang Z., Wang H., Li N. and Wang W. (2021) Spatial heterogeneity of redox-sensitive trace metal enrichments in upper ediacaran anoxic black shales. J. Geol. Soc. London 178, jgs2020-234.

Johnston D. T., Poulton S. W., Goldberg T., Sergeev V. N., Podkovyrov V., Vorob'eva N. G., Bekker A. and Knoll A. H. (2012) Late Ediacaran redox stability and metazoan evolution. Earth Planet. Sci. Lett. 335, 25–35.

Johnston D. T., Poulton S. W., Tosca N. J., O'Brien T., Halverson G. P., Schrag D. P. and Macdonald F. A. (2013) Searching for an oxygenation event in the fossiliferous Ediacaran of northwestern Canada. Chem. Geol. 362, 273–286.

Kaufman A. J., Jiang G., Christie-Blick N., Banerjee D. M. and Rai V. (2006) Stable isotope record of the terminal Neoproterozoic Krol platform in the Lesser Himalayas of northern India. Precambrian Res. 147, 156–185.

Kendall B., Dahl T. W. and Anbar A. D. (2017) The stable isotope geochemistry of molybdenum. Rev. Mineral. Geochem. 82, 683–732.

Kendall B., Komiya T., Lyons T. W., Bates S. M., Gordon G. W., Romaniello S. J., Jiang G., Creaser R. A., Xiao S., McFadden K., Sawaki Y., Tahata M., Shu D., Han J., Li Y., Chu X. and Anbar A. D. (2015) Uranium and molybdenum isotope evidence for an episode of widespread ocean oxygenation during the late Ediacaran Period. Geochim. Cosmochim. Acta 156, 173–193.

Kerl C. F., Lohmayer R., Bura-Nakić E., Vance D. and Planer-Friedrich B. (2017) Experimental Confirmation of Isotope Fractionation in Thiomolybdates Using Ion Chromatographic Separation and Detection by Multicollector ICPMS. Anal. Chem. 89, 3123–3129.

Knoll, A.H. (2011) The multiple origins of complex multicellularity. Annu. Rev. Earth Planet. Sci. 39, 217-239.

Knoll A. H. and Carroll S. B. (1999) Early animal evolution: Emerging views from comparative biology and geology. Science 284, 2129–2137.

Kurzweil F., Drost K., Pašava J., Wille M., Taubald H., Schoeckle D. and Schoenberg R. (2015) Coupled sulfur, iron and molybdenum isotope data from black shales of the Teplá-Barrandian unit argue against deep ocean oxygenation during the Ediacaran. Geochim. Cosmochim. Acta 171, 121–142.

Laakso T. A. and Schrag D. P. (2020) The role of authigenic carbonate in Neoproterozoic carbon isotope excursions. Earth Planet. Sci. Lett. 549, 116534.

Lenton T. M., Boyle R. A., Poulton S. W., Shields-Zhou G. A. and Butterfield N. J. (2014) Co-evolution of eukaryotes and ocean oxygenation in the Neoproterozoic era. Nature Geoscience 7, 257–265.

Li C., Love G. D., Lyons T. W., Fike D. A., Sessions A. L. and Chu X. (2010) A stratified redox model for the ediacaran ocean. Science 328, 80–83.

Li C., Planavsky N. J., Shi W., Zhang Z., Zhou C., Cheng M., Tarhan L. G., Luo G. and Xie S. (2015) Ediacaran Marine Redox Heterogeneity and Early Animal Ecosystems. Scientific Reports 5, 1–8.

Li J., Liang X. R., Zhong L. F., Wang X. C., Ren Z. Y., Sun S. L., Zhang Z. F. and Xu J. F. (2014) Measurement of the Isotopic Composition of Molybdenum in Geological Samples by MC-ICP-MS using a Novel Chromatographic Extraction Technique. Geostand. Geoanal. Res. 38, 345–354.

Lu M., Zhu M., Zhang J., Shields-Zhou G., Li G., Zhao F., Zhao X. and Zhao M. (2013) The DOUNCE event at the top of the Ediacaran Doushantuo Formation, South China: Broad stratigraphic occurrence and non-diagenetic origin. Precambrian Res. 225, 86–109.

Lyons, T.W., Anbar, A.D., Severmann, S., Scott, C. and Gill, B.C. (2009) Tracking euxinia in the ancient ocean: a multiproxy perspective and Proterozoic case study. Annu. Rev. Earth Planet. Sci. 37, 507–534.

Lyons T. W., Reinhard C. T. and Planavsky N. J. (2014) The rise of oxygen in Earth's early ocean and atmosphere. Nature 506, 307–315.

Lyons T. W. and Severmann S. (2006) A critical look at iron paleoredox proxies: New insights from modern euxinic marine basins. Geochim Cosmochim Acta 70, 5698–5722.

März C., Poulton S. W., Beckmann B., Küster K., Wagner T. and Kasten S. (2008) Redox sensitivity of P cycling during marine black shale formation: Dynamics of sulfidic and anoxic, non-sulfidic bottom waters. Geochim. Cosmochim. Acta 72, 3703–3717.

Massey M. S., Lezama-Pacheco J. S., Jones M. E., Ilton E. S., Cerrato J. M., Bargar J. R. and Fendorf S. (2014) Competing retention pathways of uranium upon reaction with Fe(II). Geochim. Cosmochim. Acta 142, 166–185.

Matthews J. J., Liu A. G., Yang C., McIlroy D., Levell B. and Condon D. J. (2021) A Chronostratigraphic Framework for the Rise of the Ediacaran Macrobiota: New Constraints from Mistaken Point Ecological Reserve, Newfoundland. GSA Bulletin 133, 612–624.

McFadden K. A., Huang J., Chu X., Jiang G., Kaufman A. J., Zhou C., Yuan X. and Xiao S. (2008) Pulsed oxidation and biological evolution in the Ediacaran Doushantuo Formation. Proc. Natl. Acad. Sci. 105, 3197–3202.

McLennan S. M. (2001) Relationships between the trace element composition of sedimentary rocks and upper continental crust. Geochem. Geophys. Geosyst. 2, 2000GC000109.

Miller A. J., Strauss J. v., Halverson G. P., Macdonald F. A., Johnston D. T. and Sperling E. A. (2017) Tracking the onset of Phanerozoic-style redox-sensitive trace metal enrichments: New results from basal Ediacaran post-glacial strata in NW Canada. Chem. Geol. 457, 24–37.

Miller C. A., Peucker-Ehrenbrink B., Walker B. D. and Marcantonio F. (2011) Re-assessing the surface cycling of molybdenum and rhenium. Geochim. Cosmochim. Acta 75, 7146–7179.

Morford J.L., Emerson, S. (1999) The geochemistry of redox sensitive trace metals in sediments. Geochim. Cosmochim. Acta 63, 1735–1750.

Morford J. L., Emerson S. R., Breckel E. J. and Kim S. H. (2005) Diagenesis of oxyanions (V, U, Re, and Mo) in pore waters and sediments from a continental margin. Geochim. Cosmochim. Acta 69, 5021–5032.

Nägler T. F., Anbar A. D., Archer C., Goldberg T., Gordon G. W., Greber N. D., Siebert C., Sohrin Y. and Vance D. (2014) Proposal for an International Molybdenum Isotope Measurement Standard and Data Representation. Geostand. Geoanal. Res. 38, 149–151.

Nägler T. F., Neubert N., Böttcher M. E., Dellwig O. and Schnetger B. (2011) Molybdenum isotope fractionation in pelagic euxinia: Evidence from the modern Black and Baltic Seas. Chem. Geol. 289, 1–11.

Nakagawa Y., Takano S., Firdaus M. L., Norisuye K., Hirata T., Vance D. and Sohrin Y. (2012) The molybdenum isotopic composition of the modern ocean. Geochem. J. 46, 131–141.

Narbonne G. M. (2004) Modular construction of early Ediacaran complex life forms. Science 305, 1141–1144.

Narbonne G. M. (2005) The Ediacara biota: Neoproterozoic origin of animals and their ecosystems. Annu. Rev. Earth Planet. Sci. 33, 421–463.

Narbonne, G.M., Laflamme, M., Greentree, C. and Trusler, P. (2009) Reconstructing a lost world: Ediacaran rangeomorphs from Spaniard's Bay, Newfoundland. J. Paleontol. 83, 503–523.

Neubert N., Nägler T. F. and Böttcher M. E. (2008) Sulfidity controls molybdenum isotope fractionation into euxinic sediments: Evidence from the modern Black Sea. Geology 36, 775–778.

Nielsen S. G. (2020) Vanadium Isotopes: A Proxy for Ocean Oxygen Variations (Elements in Geochemical Tracers in Earth System Science). Cambridge University Press.

Noordmann J., Weyer S., Montoya-Pino C., Dellwig O., Neubert N., Eckert S., Paetzel M. and Böttcher

M. E. (2015) Uranium and molybdenum isotope systematics in modern euxinic basins: Case studies from the central Baltic Sea and the Kyllaren fjord (Norway). Chem. Geol. 396, 182–195.

Och L. M., Cremonese L., Shields-Zhou G. A., Poulton S. W., Struck U., Ling H., Li D., Chen X., Manning C., Thirlwall M., Strauss H. and Zhu M. (2016) Palaeoceanographic controls on spatial redox distribution over the Yangtze Platform during the Ediacaran–Cambrian transition. Sedimentology 63, 378–410.

Och L. M. and Shields-Zhou G. A. (2012) The Neoproterozoic oxygenation event: Environmental perturbations and biogeochemical cycling. Earth Sci. Rev. 110, 26–57.

Ostrander C. M., Sahoo S. K., Kendall B., Jiang G., Planavsky N. J., Lyons T. W., Nielsen S. G., Owens J. D., Gordon G. W., Romaniello S. J. and Anbar A. D. (2019) Multiple negative molybdenum isotope excursions in the Doushantuo Formation (South China) fingerprint complex redox-related processes in the Ediacaran Nanhua Basin. Geochim. Cosmochim. Acta 261, 191–209.

Ouyang Q., Zhou C., Xiao S., Chen Z. and Shao Y. (2019) Acanthomorphic acritarchs from the Ediacaran Doushantuo Formation at Zhangcunping in South China, with implications for the evolution of early Ediacaran eukaryotes. Precambrian Res. 320, 171–192.

Poulson Brucker R.L., McManus J., Severmann S., Berelson W.M. (2009) Molybdenum behavior during early diagenesis: Insights from Mo isotopes. Geochem. Geophys. Geosyst. 10, Q06010.

Poulton S. W. (2021) The Iron Speciation Paleoredox Proxy. (Elements in Geochemical Tracers in Earth System Science). Cambridge University Press.

Poulton S. W. and Canfeld D. E. (2011) Ferruginous Conditions: A Dominant Feature of the Ocean through Earth's History. Elements 7, 107–112.

Poulton S. W. and Canfield D. E. (2005) Development of a sequential extraction procedure for iron: implications for iron partitioning in continentally derived particulates. Chem. Geol. 214, 209–221.

Poulton S. W., Fralick P. W. and Canfield D. E. (2004) The transition to a sulphidic ocean ~ 1.84 billion years ago. Nature 431, 173–177.

Poulton S. W. and Raiswell R. (2002) The low-temperature geochemical cycle of iron: From continental fluxes to marine sediment deposition. Am. J. Sci. 302, 774–805.

Prave A. R., Condon D. J., Hoffmann K. H., Tapster S. and Fallick A. E. (2016) Duration and nature of the end-Cryogenian (Marinoan) glaciation. Geology 44, 631–634.

Qu Y., Zhu S., Whitehouse M., Engdahl A. and McLoughlin N. (2018) Carbonaceous biosignatures of the earliest putative macroscopic multicellular eukaryotes from 1630 Ma Tuanshanzi Formation, north China. Precambrian Res. 304, 99–109.

Raiswell R. and Canfield D. E. (1998) Sources of iron for pyrite formation in marine sediments. Am. J. Sci. 298, 219–245.

Raiswell R., Newton R. and Wignall P. B. (2001) An Indicator of Water-Column Anoxia: Resolution of Biofacies Variations in the Kimmeridge Clay (Upper Jurassic, U.K.). J. Sediment. Res. 71, 286–294.

Rooney A. D., Cantine M. D., Bergmann K. D., Gómez-Pérez I., Baloushi B. al, Boag T. H., Busch J. F., Sperling E. A. and Strauss J. v. (2020) Calibrating the coevolution of Ediacaran life and environment. Proc. Natl. Acad. Sci. 117, 16824–16830.

Rooney A. D., Strauss J. v., Brandon A. D. and Macdonald F. A. (2015) A Cryogenian chronology: Two long-lasting synchronous Neoproterozoic glaciations. Geology 43, 459–462.

Rothman D. H., Hayes J. M. and Summons R. E. (2003) Dynamics of the Neoproterozoic carbon cycle. Proc. Natl. Acad. Sci. 100, 8124–8129.

Sahoo S. K., Planavsky N. J., Jiang G., Kendall B., Owens J. D., Wang X., Shi X., Anbar A. D. and Lyons T. W. (2016) Oceanic oxygenation events in the anoxic Ediacaran ocean. Geobiology 14, 457–468.

Sahoo S. K., Planavsky N. J., Kendall B., Wang X., Shi X., Scott C., Anbar A. D., Lyons T. W. and Jiang G. (2012) Ocean oxygenation in the wake of the Marinoan glaciation. Nature 489, 546–549.

Scholz F., McManus J. and Sommer S. (2013) The manganese and iron shuttle in a modern euxinic basin and implications for molybdenum cycling at euxinic ocean margins. Chem. Geol. 355, 56–68.

Scholz F., Siebert C., Dale A. W. and Frank M. (2017) Intense molybdenum accumulation in sediments underneath a nitrogenous water column and implications for the reconstruction of paleo-redox conditions based on molybdenum isotopes. Geochim. Cosmochim. Acta 213, 400–417.

Schrag D. P., Higgins J. A., Macdonald F. A. and Johnston D. T. (2013) Authigenic carbonate and the history of the global carbon cycle. Science 339, 540–543.

Scott C. and Lyons T. W. (2012) Contrasting molybdenum cycling and isotopic properties in euxinic versus non-euxinic sediments and sedimentary rocks: Refining the paleoproxies. Chem. Geol. 324–325, 19–27.

Scott C., Lyons T. W., Bekker A., Shen Y., Poulton S. W., Chu X. and Anbar A. D. (2008) Tracing the stepwise oxygenation of the Proterozoic ocean. Nature 452, 456–459.

Scott C., Slack J. F. and Kelley K. D. (2017) The hyper-enrichment of V and Zn in black shales of the Late Devonian-Early Mississippian Bakken Formation (USA). Chem. Geol. 452, 24–33.

Shi W., Li C., Luo G., Huang J., Algeo T. J., Jin C., Zhang Z. and Cheng M. (2018) Sulfur isotope evidence

for transient marine-shelf oxidation during the Ediacaran Shuram Excursion. Geology 46, 267–270.

Shields G. A., Mills B. J. W., Zhu M., Raub T. D., Daines S. J. and Lenton T. M. (2019) Unique Neoproterozoic carbon isotope excursions sustained by coupled evaporite dissolution and pyrite burial. Nature Geoscience 12, 823–827.

Shields-Zhou G., Och L., (2011) The case for a Neoproterozoic oxygenation event: geochemical evidence and biological consequences. GSA Today 21, 4–11.

Sperling E. A., Frieder C. A., Raman A. v., Girguis P. R., Levin L. A. and Knoll A. H. (2013) Oxygen, ecology, and the Cambrian radiation of animals. Proc. Natl. Acad. Sci. 110, 13446–13451.

Sperling E. A., Wolock C. J., Morgan A. S., Gill B. C., Kunzmann M., Halverson G. P., Macdonald F. A., Knoll A. H. and Johnston D. T. (2015) Statistical analysis of iron geochemical data suggests limited late Proterozoic oxygenation. Nature 523, 451–454.

Summons R. E., Bradley A. S., Jahnke L. L. and Waldbauer J. R. (2006) Steroids, triterpenoids and molecular oxygen. Philosophical Transactions of the Royal Society B: Biological Sciences 361, 951–968.

Tossell J. A. (2005) Calculating the partitioning of the isotopes of Mo between oxidic and sulfidic species in aqueous solution. Geochim. Cosmochim. Acta 69, 2981–2993.

Tostevin R., Clarkson M. O., Gangl S., Shields G. A., Wood R. A., Bowyer F., Penny A. M. and Stirling C. H. (2019) Uranium isotope evidence for an expansion of anoxia in terminal Ediacaran oceans. Earth Planet. Sci. Lett. 506, 104–112.

Tostevin R. and Mills B. J. W. (2020) Reconciling proxy records and models of Earth's oxygenation during the Neoproterozoic and Palaeozoic. Interface Focus 10. 20190137

Tribovillard N., Algeo T. J., Baudin F. and Riboulleau A. (2012) Analysis of marine environmental conditions based onmolybdenum–uranium covariation—Applications to Mesozoic paleoceanography. Chem. Geol. 324–325, 46–58.

Tribovillard N., Algeo T. J., Lyons T. and Riboulleau A. (2006) Trace metals as paleoredox and paleoproductivity proxies: An update. Chem. Geol. 232, 12–32.

Tribovillard N., Bout-Roumazeilles V., Algeo T., Lyons T. W., Sionneau T., Montero-Serrano J. C., Riboulleau A. and Baudin F. (2008) Paleodepositional conditions in the Orca Basin as inferred from organic matter and trace metal contents. Mar. Geol. 254, 62–72.

Wang J. and Li Z. X. (2003) History of Neoproterozoic rift basins in South China: implications for Rodinia break-up. Precambrian Res. 122, 141–158.

Wanty R. B. and Goldhaber M. B. (1992) Thermodynamics and kinetics of reactions involving

vanadium in natural systems: Accumulation of vanadium in sedimentary rocks. Geochim. Cosmochim. Acta 56, 1471–1483.

Warren L. v., Pacheco M. L. A. F., Fairchild T. R., Simões M. G., Riccomini C., Boggiani P. C. and Cáceres A. A. (2012) The dawn of animal skeletogenesis: Ultrastructural analysis of the Ediacaran metazoan Corumbella werneri. Geology 40, 691–694.

Wedepohl K.H. (1995) The composition of the continental crust. Geochim. Cosmochim. Acta 59, 1217–1232.

Wei G. Y., Planavsky N. J., He T., Zhang F., Stockey R. G., Cole D. B., Lin Y. B. and Ling H. F. (2021) Global marine redox evolution from the late Neoproterozoic to the early Paleozoic constrained by the integration of Mo and U isotope records. Earth Sci. Rev. 214, 103506.

Wen H., Fan H., Zhang Y., Cloquet C. and Carignan J. (2015) Reconstruction of early Cambrian ocean chemistry from Mo isotopes. Geochim Cosmochim Acta 164, 1–16.

Willbold M. and Elliott T. (2017) Molybdenum isotope variations in magmatic rocks. Chem. Geol. 449, 253–268.

Wood R. A., Poulton S. W., Prave A. R., Hoffmann K. H., Clarkson M. O., Guilbaud R., Lyne J. W., Tostevin R., Bowyer F., Penny A. M., Curtis A. and Kasemann S. A. (2015) Dynamic redox conditions control late Ediacaran metazoan ecosystems in the Nama Group, Namibia. Precambrian Res. 261, 252–271.

Wu Y., Tian H., Li J., Li T. and Ji S. (2021) Reconstruction of oceanic redox structures during the Ediacaran-Cambrian transition in the Yangtze Block of South China: Implications from Mo isotopes and trace elements. Precambrian Res. 359, 106181.

Xiao S., Chen Z., Pang K., Zhou C. and Yuan X. (2021) The shibantan lagerstätte: Insights into the proterozoic– phanerozoic transition. J. Geol. Soc. London 178, jgs2020-135.

Xiao S., Knoll A. H., Yuan X. and Pueschel C. M. (2004) Phosphatized multicellular algae in the Neoproterozoic Doushantuo Formation, China, and the early evolution of florideophyte red algae. Am. J. Bot. 91, 214–227.

Xiao S., Laflamme M. (2009) On the eve of animal radiation: phylogeny, ecology and evolution of the Ediacara biota. Trends Ecol. Evol. 24, 31–40.

Xiao S.H., Narbonne G.M. (2020) The Ediacaran Period. In: Gradstein, F.M., Ogg, J.G., Schmitz, M.D., Ogg, G.M. (Eds.), Geological Time Scale 2020. Elsevier BV Amsterdam.

Xiao S., Shen B., Zhou C., Xie G. and Yuan X. (2005) A uniquely preserved Ediacaran fossil with direct evidence for a quilted bodyplan. Proc. Natl. Acad. Sci. 102, 10227–10232.

Xiao S., Zhou C., Liu P., Wang D. and Yuan X. (2014) Phosphatized Acanthomorphic Acritarchs and Related Microfossils from the Ediacaran Doushantuo Formation at Weng'an (South China) and their Implications for Biostratigraphic Correlation. J. Paleontol. 88, 1–67.

Xiong Y., Guilbaud R., Peacock C. L., Cox R. P., Canfield D. E., Krom M. D. and Poulton S. W. (2019) Phosphorus cycling in Lake Cadagno, Switzerland: A low sulfate euxinic ocean analogue. Geochim. Cosmochim. Acta 251, 116–135.

Xu D., Wang Xinqiang, Zhu J. M., Jiang G., Shi X., Wang Xiangli and Sahoo S. K. (2022) Chromium isotope evidence for oxygenation events in the Ediacaran ocean. Geochim. Cosmochim. Acta 323, 258–275.

Yang C., Rooney A. D., Condon D. J., Li X. H., Grazhdankin D. v., Bowyer F. T., Hu C., Macdonald F. A. and Zhu M. (2021) The tempo of Ediacaran evolution. Sci. Adv. 7, eabi9643.

Ye Y., Wang H., Wang X., Zhai L., Wu C., Canfield D. E. and Zhang S. (2020) Tracking the evolution of seawater Mo isotopes through the Ediacaran–Cambrian transition. Precambrian Res. 350, 105929.

Yeasmin R., Chen D., Fu Y., Wang J., Guo Z. and Guo C. (2017) Climatic-oceanic forcing on the organic accumulation across the shelf during the Early Cambrian (Age 2 through 3) in the mid-upper Yangtze Block, NE Guizhou, South China. J. Asian Earth Sci. 134, 365–386.

Yuan X., Chen Z., Xiao S., Zhou C. and Hua H. (2011) An early Ediacaran assemblage of macroscopic and morphologically differentiated eukaryotes. Nature 470, 390–393.

Zhang F., Xiao S., Kendall B., Romaniello S. J., Cui H., Meyer M., Gilleaudeau G. J., Kaufman A. J. and Anbar A. D. (2018) Extensive marine anoxia during the terminal ediacaran period. Sci. Adv. 4, eaan8983.

Zhang F., Xiao S., Romaniello S. J., Hardisty D., Li C., Melezhik V., Pokrovsky B., Cheng M., Shi W., Lenton T. M. and Anbar A. D. (2019) Global marine redox changes drove the rise and fall of the Ediacara biota. Geobiology 17, 594–610.

Zhang S., Jiang G., Zhang J., Song B., Kennedy M. J. and Christie-Blick N. (2005) U-Pb sensitive high-resolution ion microprobe ages from the Doushantuo Formation in south China: Constraints on late Neoproterozoic glaciations. Geology 33, 473–476.

Zhang Y., Wen H., Zhu C., Fan H., Xiao J. and Wen J. (2021) Molybdenum isotopic evidence for anoxic marine conditions during the end-Permian mass extinction. Chem. Geol. 575, 120259.

Zhou C., Huyskens M. H., Lang X., Xiao S. and Yin Q. Z. (2019) Calibrating the terminations of Cryogenian global glaciations. Geology 47, 251–254.

Zhu B., Jiang S., Pi D., Ge L. and Yang J. (2018) Trace Elements Characteristics of Black Shales from the

Ediacaran Doushantuo Formation, Hubei Province, South China: Implications for Redox and Open vs. Restricted Basin Conditions. J. Earth Sci. 29, 342–352.

Zhou, Y., von Strandmann, P.A.P., Zhu, M., Ling, H., Manning, C., Li, D., He, T. and Shields, G.A. (2020) Reconstructing Tonian seawater 87Sr/86Sr using calcite microspar. Geology 48, 462–467.

Zhu M., Zhang J., Steiner M., Yang A., Li G. and Erdtmann B. (2003) Sinian-Cambrian stratigraphic framework for shallow- to deep-water environments of the Yangtze Platform: an integrated approach. Prog. Nat. Sci. 13, 951–960.

Zhu, M., Zhao, F., Yin, Z., Zeng, H. and Li, G. (2019) The Cambrian explosion: Advances and perspectives from China. Sci. China Earth Sci. 49, 1455-1490.